JCB Journal of Cell Biology

ARTICLE

Excessive STAU1 condensate drives mTOR translation and autophagy dysfunction in neurodegeneration

Ruiqian Zhao[1], Shijing Huang[1], Jingyu Li[1], Aihong Gu[1], Minjie Fu[1], Wei Hua[1], Ying Mao[1], Qun-Ying Lei[2], Boxun Lu[3], and Wenyu Wen[1]

The double-stranded RNA-binding protein Staufen1 (STAU1) regulates a variety of physiological and pathological events via mediating RNA metabolism. STAU1 overabundance was observed in tissues from mouse models and fibroblasts from patients with neurodegenerative diseases, accompanied by enhanced mTOR signaling and impaired autophagic flux, while the underlying mechanism remains elusive. Here, we find that endogenous STAU1 forms dynamic cytoplasmic condensate in normal and tumor cell lines, as well as in mouse Huntington's disease knockin striatal cells. STAU1 condensate recruits target mRNA *MTOR* at its 5′UTR and promotes its translation both in vitro and in vivo, and thus enhanced formation of STAU1 condensate leads to mTOR hyperactivation and autophagy–lysosome dysfunction. Interference of STAU1 condensate normalizes mTOR levels, ameliorates autophagy–lysosome function, and reduces aggregation of pathological proteins in cellular models of neurodegenerative diseases. These findings highlight the importance of balanced phase separation in physiological processes, suggesting that modulating STAU1 condensate may be a strategy to mitigate the progression of neurodegenerative diseases with STAU1 overabundance.

Introduction

Staufen (STAU) is a double-stranded RNA (dsRNA) binding protein that was first identified in *Drosophila melanogaster*, where it regulated the transport and localization of *bicoid* and *oskar* mRNAs in oocytes and *prospero* mRNA during neuroblast (NB) asymmetric division, thus controlling embryo polarity and cell fate (Broadus et al., 1998; Li et al., 1997; Micklem et al., 2000). STAU is highly conserved during evolution, and two mammalian orthologs, STAU1 and STAU2, have been identified, which form distinct ribonucleoprotein particles (RNPs) and regulate different physiological pathways (Furic et al., 2008; Lebeau et al., 2008). STAU1 is ubiquitously expressed, and two major STAU1 isoforms, STAU1^{55} and STAU1^{63}, are generated through alternative splicing, whereas STAU2 is mainly expressed in brain and heart (Almasi and Jasmin, 2021). All STAU proteins share a common domain organization consisting of four to five dsRNA-binding domains (dsRBDs). Specifically, STAU1 has four dsRBDs, two of which (dsRBD3 and dsRBD4) are responsible for dsRNA binding (Micklem et al., 2000), followed by a microtubule-binding domain (TBD) and a STAU-swapping motif (SSM) (Gleghorn et al., 2013).

To date, there are no STAU1 knockout mice available, implying an essential role of STAU1 in development. Homozygous STAU1^{tm1Apa} mutant mice expressing a truncated STAU1 protein lacking dsRBD3 showed defects in locomotor activity, and neurons derived from these mice displayed abnormal dendritic mRNA transport and neuron morphology, accompanied by impaired synapse plasticity (Vessey et al., 2008). A similar phenotype was observed in cultured hippocampal neurons with STAU1 knockdown (KD) by RNA interference (Lebeau et al., 2008). As an essential regulator of RNA metabolism, STAU1 plays diverse roles in various cellular functions, including cell differentiation and proliferation, stress response, apoptosis, autophagy, and RNA virus replication (Boulay et al., 2014; Gandelman et al., 2020; Paul et al., 2018; Ramos et al., 2022), by controlling mRNA transport and localization, translation, Staufen-mediated mRNA decay (SMD), and splicing

[1]Department of Neurosurgery, Huashan Hospital, The Shanghai Key Laboratory of Medical Epigenetics, State Key Laboratory of Medical Neurobiology and MOE Frontiers Center for Brain Science, Institutes of Biomedical Sciences, School of Basic Medical Sciences, Fudan University, Shanghai, China; [2]Fudan University Shanghai Cancer Center and Institutes of Biomedical Sciences, Shanghai Medical College, Fudan University, Shanghai, China; [3]State Key Laboratory of Medical Neurobiology and MOE Frontiers Center for Brain Science, New Cornerstone Science Laboratory, School of Life Sciences, Fudan University, Shanghai, China.

Correspondence to Wenyu Wen: wywen@fudan.edu.cn.

(Dugré-Brisson et al., 2005; Gleghorn et al., 2013; Kim et al., 2005; Ravel-Chapuis et al., 2012; Ricci et al., 2014; Vessey et al., 2008). A previous study has identified more than 260 transcripts significantly up- or downregulated in STAU1-depleted human neuroblastoma cell line SH-SY5Y cells by mRNA-seq analysis (Oh et al., 2018). High-throughput studies have revealed different classes of STAU1-binding sites (SBS) located in double-stranded regions (Laver et al., 2013; Ricci et al., 2014; Sugimoto et al., 2015). STAU1 can enhance the translation of a specific mRNA population that contains an SBS in the 5′UTR or coding sequence regions with high GC content (Dugré-Brisson et al., 2005; Ricci et al., 2014). On the other hand, STAU1 recruitment to the 3′UTR of target mRNA elicits the SMD pathway to promote RNA degradation (Gong and Maquat, 2011; Kim et al., 2005) or prevents its translation (de Morrée et al., 2017; Elbarbary et al., 2013). It is noteworthy that STAU1 may up- or downregulate various genes simultaneously in a single cellular pathway, thus balancing their expression and achieving optimal cell functions. However, how STAU1 efficiently regulates so many target mRNAs remains elusive.

Recently, the role of STAU1 in neurodegeneration has emerged. Most neurodegenerative diseases exhibit severe aggregation of misfolded proteins in different regions of the brain (Ross and Poirier, 2004). Such aggregates generally could only be recognized by macroautophagy for degradation but not the ubiquitin-proteasome system or chaperone-mediated autophagy; thus macroautophagy has been regarded as an effective neuroprotective mechanism to clear these pathogenic and toxic proteins such as α-synuclein, TDP-43, tau, and huntingtin (Ciechanover and Kwon, 2015; Fleming et al., 2022; Zhao et al., 2021). However, the pathological progression of neurodegenerative diseases indicates that autophagy might reach a saturation point beyond its ability to degrade the aggregate-prone mutant proteins, or that the autophagy pathway might be defective (Levine and Kroemer, 2008; Menzies et al., 2017). Therefore, autophagy dysfunction is a hallmark of neurodegenerative diseases in which misfolded proteins accumulate. A recent study showed that substantial increase of STAU1 level was observed in patient fibroblasts and tissues from animal models of many human neurodegenerative diseases, including spinocerebellar ataxia type 2 (SCA2), amyotrophic lateral sclerosis (ALS), frontotemporal dementia (FTD), Huntington's and Alzheimer's diseases (HD and AD), accompanied with hyperactivation of mTOR signaling and autophagy dysfunction (Paul et al., 2021). Moreover, STAU1 depletion was found to reduce the accumulation of mutant ATXN2 protein and ameliorate disease phenotype in mice model of spinocerebellar ataxia type2 (SCA2) (Paul et al., 2018), a progressive autosomal dominantly inherited neurodegenerative disease caused by CAG repeat expansion in *ATXN2* (Paulson et al., 2017). Whether STAU1 overabundance is an accompanied result of aberrant autophagy or it actively participates in the development of various neurodegenerative diseases (with unknown mechanisms) is an open question. Furthermore, as STAU1 regulates the destiny of hundreds of target mRNAs, if it has therapeutic potential, a more specific strategy to manipulate STAU1 function relevant to neurodegenerative processes is urgently needed.

Here, endogenous STAU1 is observed to undergo liquid-liquid phase separation (LLPS) (Alberti and Hyman, 2021; Banani et al., 2017; Chen et al., 2020; Lafontaine et al., 2021; Mayr et al., 2023; Zhang et al., 2020; Zheng and Wen, 2023) to form enriched and dynamic condensate in distinct cell lines including tumor cells and mouse HD striatal cells. Of note, label-free protein quantification by mass spectrometry is used for the analysis of U251 human glioma cells expressed with wild type (WT) or LLPS-deficient mutant of STAU1. The results show that a subset of proteins including mTOR are upregulated in cells expressing STAU1 in a LLPS-dependent manner. 5′UTR of *MTOR* mRNA could be recruited into STAU1 condensate, which further promotes STAU1 phase separation, whereas *MTOR* mRNA translation efficiency is significantly enhanced within STAU1 condensate. Consequently, STAU1 condensate-induced elevation of mTOR, a master regulator of autophagy, impairs autophagic flux and lysosomal function. Moreover, dampening STAU1 LLPS reduces the mTOR activity to a normal state, restores the autophagy-lysosome pathway, and subsequently ameliorates the aggregation of pathological proteins in cell models of neurodegenerative diseases.

Results

Endogenous STAU1 exhibited punctate distribution in the cytoplasm

Essential for mRNA transport and localization, STAU1 was found to organize RNA-containing granules destined for dendritic spines in mature hippocampal neurons (Mitsumori et al., 2017; Vessey et al., 2008). Several studies revealed that STAU1 could be recruited into stress granules (SGs) under stress in several cell types including oligodendrocytes and hippocampal neurons (Paul et al., 2018; Thomas et al., 2009). As a ubiquitously expressed RNA-binding protein, we wondered how STAU1 is subcellularly distributed in the steady state in different cell lines. Immunostaining using anti-STAU1 antibodies revealed that discrete small STAU1 puncta could be observed in the cytoplasm of African green monkey kidney COS7 cells and human cell lines including embryonic kidney HEK-293T cells, neurologic tumor cells (U251, SH-SY5Y) as well as other cancer cells (cervical Hela, liver HepG2, pancreatic SW1990, colonic Caco-2) (Fig. 1 A and Fig. S1 A). It is worth noting that STAU1 levels in HepG2, SW1990, as well as Caco-2 cells were dramatically higher than those in other cells; correspondingly, the puncta sizes of endogenous STAU1 in the three cancer cells were also significantly larger (Fig. 1, A–C). In line with the observation that higher STAU1 levels were correlated with upregulated mTOR signal in FB cells from patients with neurodegenerative diseases and tissues from mouse models (Paul et al., 2021; Paul et al., 2023), mTOR and p-mTOR levels in HepG2, SW1990, and Caco-2 cells were found to be the highest among all tested cell lines (Fig. 1 C and Fig. S1 B).

The above observation suggests a potential connection between enlarged cytoplasmic STAU1 puncta and upregulation of STAU1 and mTOR levels. We assumed this phenomenon might also exist in cells from mouse models of neurodegenerative diseases with elevated STAU1. To test this hypothesis, we

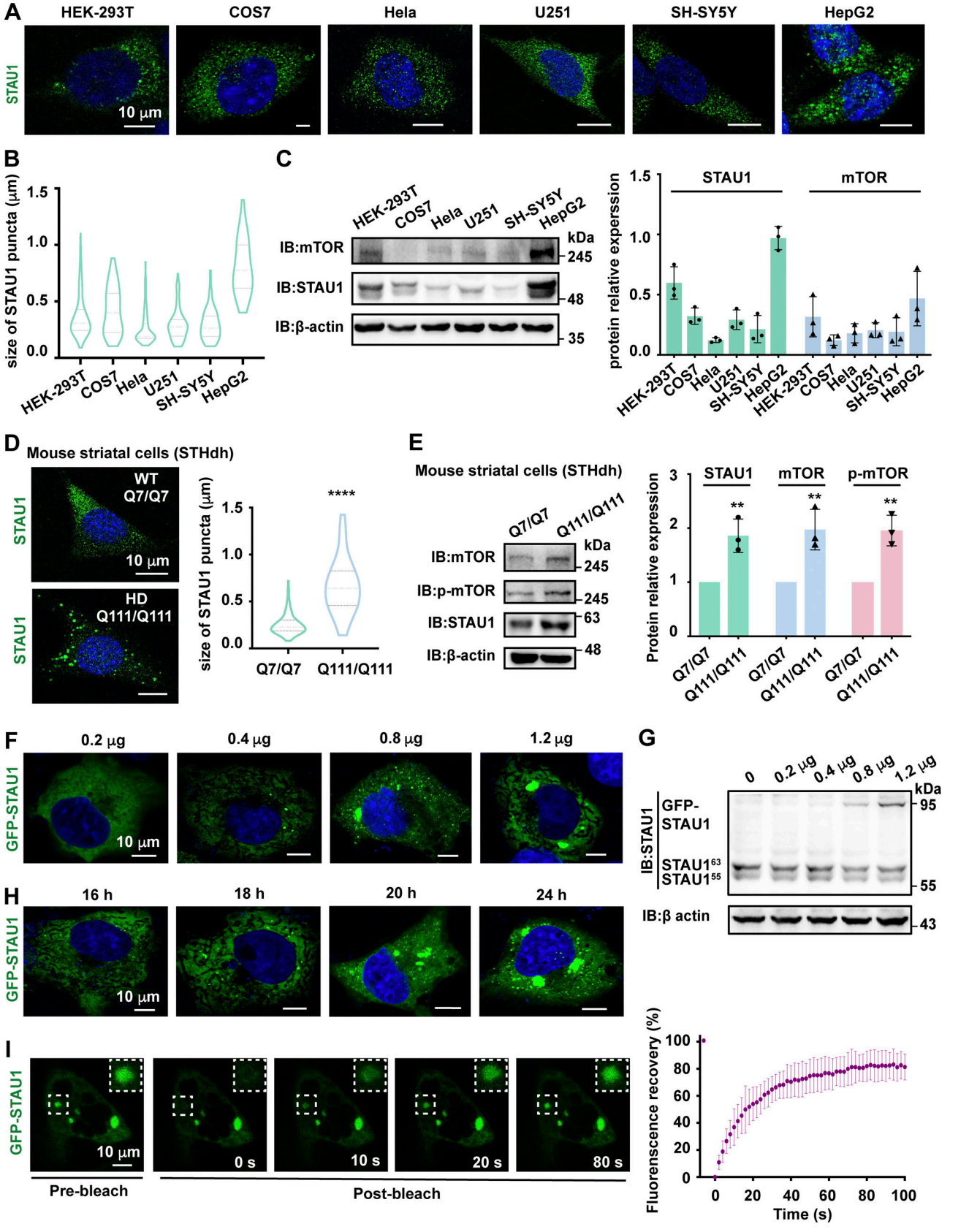

Figure 1. **STAU1 undergoes LLPS in living cells. (A)** Representative immunostaining images of 293T cells, COS7 cells, Hela cells, U251 cells, SH-SY5Y cells, and HepG2 cells with STAU1 antibody. Scale bars: 10 μm. **(B)** Statistical data for the sizes of endogenous STAU1 puncta in A. >200 puncta were counted for each batch. **(C)** Left: Representative immunoblotting images measuring the expression levels of endogenous STAU1 and mTOR in various cell lines. Right:

Quantitative analysis of the WB assay is normalized by β-actin. Data are presented as the mean ± SD of triplicate experiments. **(D)** Left: Representative images of endogenous STAU1 in mouse striatal WT STHdh$^{Q7/Q7}$ and HD STHdh$^{Q111/Q111}$ cells. Scale bar: 10 µm. Right: Statistical data for the sizes of endogenous STAU1 puncta. >200 puncta were counted for each batch. ****P < 0.0001 using one-way ANOVA with Tukey's multiple comparison test. **(E)** Left: Representative WB assay images of STHdh cells showing the increased levels of STAU1, mTOR, and p-mTOR in STHdhQ111/Q111 cells. Protein levels were normalized to β-actin. Right: Quantification of average fold changes for STAU1, mTOR, and p-mTOR. Data are presented as the mean ± SD of triplicate experiments; **P < 0.01 using one-way ANOVA with Tukey's multiple comparison test. **(F)** Representative images showing the concentration-dependent formation of GFP-STAU1 puncta in COS7 cells. Cells were transfected with increased amounts of GFP-STAU1 plasmid (0.2, 0.4, 0.8, 1.2 µg per well in a 12-well plate). Scale bar: 10 µm. **(G)** Representative WB assay images showing the expression levels of GFP-STAU1 and endogenous STAU1. Increased amounts of GFP-STAU1 plasmid (0.2, 0.4, 0.8, 1.2 µg per well in a 12-well plate) were transfected into COS7 cells. **(H)** Representative images of STAU1 condensation in COS7 cells transfected with 0.8 µg GFP-STAU1 plasmid at different transfection time points ranging from 16 to 24 h. Scale bar: 10 µm. **(I)** Left: Representative confocal images of the FARP analysis of GFP-STAU1 puncta in COS7 cells. Scale bar: 10 µm. Right: The purple curve represents the averaged FRAP data of 15 puncta from 15 cells. Time 0 refers to the time point of the photobleaching pulse. All data are represented as mean ± SD.

investigated the localization and protein level of STAU1 in the mouse HD knockin striatal STHdh$^{Q111/Q111}$ cells, a well-established cellular model for HD (Trettel et al., 2000). HD is a fatal progressive neurodegenerative disorder caused by an autosomal dominant mutation with an expansion of more than 35 trinucleotide CAG repeats (which codes for polyglutamine) in exon 1 of the huntingtin gene (*HTT*) (Tabrizi et al., 2019). Thus, HD pathogenesis is frequently modeled with exon-1 fragments containing expanded polyQ repeats, which generate neurotoxic aggregates in cell models and in vivo. In comparison with wild type STHdh$^{Q7/Q7}$ cells, STHdh$^{Q111/Q111}$ expresses full-length *mHtt* (the mouse homolog of human *HTT*) with 111Q repeats. As expected, endogenous STAU1 showed dense and small puncta in WT STHdh$^{Q7/Q7}$ cells, while larger and more obvious STAU1 puncta were observed in HD STHdh$^{Q111/Q111}$ cells (Fig. 1 D). Consistent with a previous report (Paul et al., 2021), levels of STAU1 proteins were significantly elevated in HD cells (Fig. 1 E; ∼twofold compared with those in WT cells). A similar elevation of mTOR and phospho-mTOR (p-mTOR) was observed in HD cells, implying a potential functional correlation of STAU1 puncta size with mTOR levels.

STAU1 could form dynamic condensates in cells

To characterize the biophysical property of those STAU1 puncta, green fluorescent protein (GFP)-tagged STAU1 was expressed from low to high levels in COS7 cells through transfection with different amounts of cDNA encoding GFP-STAU1 for 20 h (Fig. 1, F and G). When GFP-STAU1 was expressed at a low level (with 0.2 µg plasmid DNA), GFP-STAU1 displayed even dispersion within cells. A few small spherical GFP-STAU1 foci formed in the cytosol of cells expressing 0.4 µg plasmid DNA (Fig. 1 F). When GFP-STAU1 was expressed at levels comparable with endogenous STAU1 (with 0.8 µg plasmid DNA), the spherical foci became bigger and brighter (Fig. 1, F and G). Similarly, a longer transfection duration of GFP-STAU1 led to enhanced formation of condensed puncta in the cytoplasm (Fig. 1 H).

We then performed fluorescence recovery after the photobleaching (FRAP) analysis to examine the dynamic properties of the above STAU1 puncta. GFP-STAU1 in the condensed puncta exhibited a rapid dynamic equilibrium with the proteins in the surrounding cytoplasm (∼60% recovery within ∼20 s, Fig. 1 I), suggesting liquid-like properties for these STAU1 spherical structures. These data indicate that STAU1 might undergo concentration-dependent LLPS in living cells.

Phase separation of STAU1 in vitro

Next, we wondered whether STAU1 alone is sufficient to form dynamic condensate in vitro. When observing recombinant STAU1 proteins with various concentrations under differential interference contrast (DIC) microscope, we noticed the appearance of spherical droplets with distinct diameters, a phenomenon characteristic of LLPS (Li et al., 2012; Liu et al., 2020) (Fig. 2, A and B). When the protein concentration increased, the size of liquid droplets also progressively increased (Fig. 2 B). Through separating the condensed phase from the aqueous phase by centrifugation, we found the liquid phase fraction of STAU1 proteins increased in a concentration-dependent manner (Fig. S1 C). STAU1 liquid phase could be observed at a relatively low concentration at ∼0.5 µM (Fig. 2 B and Fig. S1 C). These STAU1 droplets autonomously fused into larger ones over time (Fig. 2 C). FRAP analysis further revealed the internal fluidity of STAU1 droplets (Fig. 2 D).

To map out the minimal functional unit of STAU1 LLPS, various recombinant STAU1 fragments containing single or tandem RBD domains were prepared and assessed by DIC microscope observation and sedimentation assay at the same protein concentration (Fig. 2, A and E; and Fig. S1 D). We found that the isolated RBD domain remained in clear aqueous solutions. RBD45 was insufficient to initiate LLPS; instead, a condensed liquid phase robustly formed for STAU1 fragments containing RBD23 (e.g., WT, RBD2345, RBD23). Deletion of either RBD2 or RBD3 dramatically impaired LLPS of STAU1 while deletion of both RBD2 and RBD3 abolished the condense phase of STAU1, demonstrating the critical role of RBD23 for phase separation of STAU1 and that the interdomain interaction of the tandem was required for the process.

Electrostatic interaction–dependent LLPS of STAU1

Next, we evaluated the detailed molecular mechanism of STAU1 LLPS. The addition of 1,6-hexanediol (1,6-HD), an aliphatic molecule that disrupts hydrophobic interaction-induced phase separation (Li et al, 2023a, 2023b), only partially weakened the STAU1 droplet formation, whereas STAU1 LLPS appeared to be more sensitive to salt conditions and that high salt concentrations (500 mM NaCl) abolished the LLPS process (Fig. 2 F and Fig. S1, E–I). Thus, STAU1 phase separation seems to be driven by both electrostatic and hydrophobic interactions from residues in RBD23, with electrostatic interaction as the dominant force. In line with this analysis, obvious positive/negative

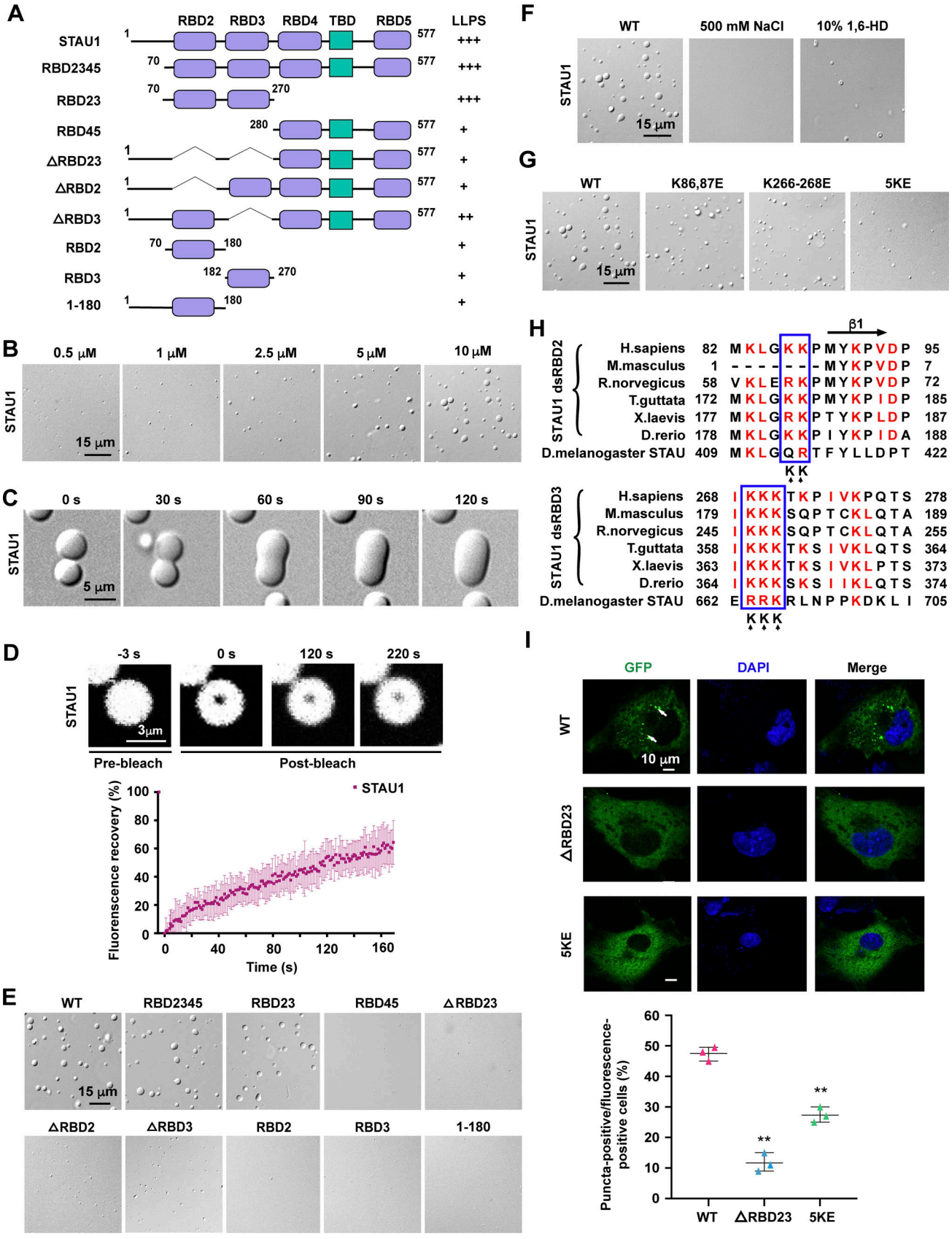

Figure 2. **Phase separation of STAU1 in vitro. (A)** Schematic diagrams showing the domain organization of STAU1. **(B)** Representative images showing protein concentration-dependent LLPS of STAU1. Images were acquired at 3 min after injecting the mixture into the chamber. Scale bar: 15 μm. **(C)** Representative time-lapse images showing time-dependent fusion of STAU1 liquid droplets. Scale bar: 5 μm. **(D)** Upper: Representative confocal images of the FRAP

experiment conducted on preformed Cy5-STAU1 droplets in vitro. Scale bar: 3 µm. Lower: FRAP recovery curve of Cy5-STAU1 by averaging signals of 17 droplets with similar sizes each after photobleaching. Time 0 refers to the time point of the photobleaching pulse. Data are represented as mean ± SD. **(E)** Representative confocal images of different STAU1 fragments under a DIC microscope at 10 µM. Scale bar: 15 µm. **(F)** Representative DIC images of preformed STAU1 condensate (10 µM) treated with 500 mM NaCl or 10% 1,6-hexanediol (1,6-HD). Scale bar: 15 µm. **(G)** Representative DIC images of STAU1 WT and various mutants (10 µM). Scale bar: 15 µm. The same sample of STAU1 WT was used in evaluating STAU1 concentration-dependent condensation in B, disruption with salt or 1,6-HD in F, and mutations in lysine residues in G. **(H)** Structure-based sequence alignment of STAU1 RBD23 fragment from different species. Highly conserved residues are highlighted in red. The five key lysine residues responsible for STAU1 LLPS are indicated by blue rectangles. **(I)** Upper: Representative confocal images of exogenously expressed GFP-STAU1 WT and mutants in COS7 cells. Scale bar: 10 µm. Lower: Statistical data of GFP-STAU1 puncta formation. White arrows indicate condensed puncta in the cytoplasm. Data were collected from three independent experimental cell culture batches, >300 cells counted for each batch. Specimens' statistics are presented as mean ± SD; **P < 0.01 using one-way ANOVA with Tukey's multiple comparison test.

charged clusters and hydrophobic clusters exist in RBD23 of STAU1 (Fig. S1 J).

We further identified the critical residues driving the LLPS of RBD23. STAU1 RBD2 was assumed to adopt a canonical dsRBD fold according to its high sequence similarity with STAU1 RBD3 (PDB ID: 6SDW) (Yadav et al., 2020). Based on the predicted RBD23 structure by Alphafold (Jumper et al., 2021), alanine-scanning mutagenesis was utilized to investigate the charged and aromatic residues on the surface of RBD23 but outside the RNA binding sites on their potential contribution to LLPS (Fig. S1, J and K). Though the K86,87E mutation on RBD2 or K266-268E mutation on RBD3 only partially weakened the level of STAU1 LLPS, combinational mutation of these two sites (referred to as 5KE hereafter) dramatically impaired droplet formation and reduced the condense phase fraction of STAU1 (Fig. 2 G and Fig. S1 L). Furthermore, the key residues (namely Lys86, Lys87, Lys266, Lys267, and Lys268) identified for LLPS of STAU1 are evolutionarily conserved from *Drosophila* to vertebrates (Fig. 2 H). We further verified whether the electrostatic interaction–driven LLPS of STAU1 in solution accounted for the puncta formation in living cells. Nicely correlated with in vitro studies of STAU1 phase separation (Fig. 2, E and G), exogenously expressed GFP-STAU1 ΔRBD23 mutant failed to form droplets in the cytoplasm of COS7 cells, and the 5KE mutation also caused a dramatic decrease of STAU1 puncta formation (Fig. 2 I).

Taken together, the above LLPS results in vitro and in living cells demonstrate that electrostatic interdomain interactions of RBD23 were the main driving forces for STAU1 LLPS.

STAU1 condensates recruit *MTOR*-5′UTR

Early studies have revealed that STAU1 formed membraneless RNA granules for mRNA transport along dendrites in neurons (Mitsumori et al., 2017; Vessey et al., 2008). Remarkably, LLPS has been recognized as a crucial mechanism for the organization of membraneless organelles (Banani et al., 2017). Both RNA and RNA binding proteins are important players in bimolecular condensates (Roden and Gladfelter, 2021), whereas their selected local enrichment in certain condensates also ensures the specificity and efficiency of cellular reactions. Thus, we sought to investigate whether the regulatory functions of STAU1 on RNAs are dependent on its LLPS property. When mCherry-STAU1 WT or 5KE was expressed in COS7 cells, a certain amount of endogenous RNAs (stained by a nucleic acid dye SYTO 12) were colocalized with mCherry-STAU1 or 5KE puncta, indicating that target RNA might be recruited into STAU1 condensate for further regulation (Fig. 3 A and Fig. S2 A).

We next aimed to identify the posttranscriptional process in which STAU1 condensates participate. An overabundance of STAU1 was found in fibroblasts from patients with neurodegenerative diseases (Paul et al., 2021). Our immunoblotting and immunostaining data also showed that STAU1 levels were elevated with enhanced puncta formation in mouse HD STHdh$^{Q111/Q111}$ cells (Fig. 1, D and E). Considering the essential roles of STAU1 in neural development and function (Oh et al., 2018; Vessey et al., 2008), label-free quantification by mass spectrometry was performed using lysates from U251 cells overexpressing Mock, STAU1 WT, or LLPS-deficient 5KE mutant to screen for target proteins. 282 proteins were found upregulated and 259 proteins downregulated in cells expressing STAU1 WT rather than 5KE (Tables S1 and S2). mTOR, a key regulator in autophagy (Querfurth and Lee, 2021), was found in the upregulated category, but the levels of mTOR transcripts remained unchanged upon STAU1 or STAU1 5KE overexpression (Fig. S2 B). Consistent with the mass spectrometry data, overexpression of STAU1 significantly elevated mTOR protein levels, whereas overexpression of STAU1 5KE only had a minor influence (Fig. 3 B), implying a potential role of STAU1 condensate in mTOR translation.

Numerous studies have shown that STAU1 directly interacts with the 5′UTR of target mRNAs to enhance their translation (Dugré-Brisson et al., 2005; Ricci et al., 2014), so we generated the 5′UTR of *MTOR* mRNA by in vitro transcription, and electrophoretic mobility shift assay (EMSA) results showed that STAU1 WT and the LLPS-deficient 5KE mutant bound to *MTOR* 5′UTR mRNA with similar affinities (Fig. S2 C). When mixing Cy5-tagged STAU1 with *MTOR*-5′UTR (stained by SYTO12), *MTOR*-5′UTR could be efficiently recruited and enriched into STAU1 droplets (Fig. 3 C). In contrast, the 3′UTR of *OSKAR* mRNA, one target RNA of *Drosophila* STAU (Micklem et al., 2000), rarely bound to STAU1 and could not be enriched in STAU1 condensate (Fig. S2, D and E), suggesting that STAU1 condensates selectively recruit and enrich target RNAs via specific interactions. Interestingly, the addition of an increasing amount of *MTOR*-5′UTR into STAU1 solution significantly increased the sizes of formed STAU1 droplets (Fig. S2 F). However, mixing STAU1 5KE mutant with *MTOR* 5′UTR RNA did not lead to an observable effect on its LLPS property (Fig. 3 D).

Taken together, the above findings indicated that *MTOR* 5′UTR RNA can be recruited and enriched into STAU1 condensate, which further promotes STAU1 phase separation.

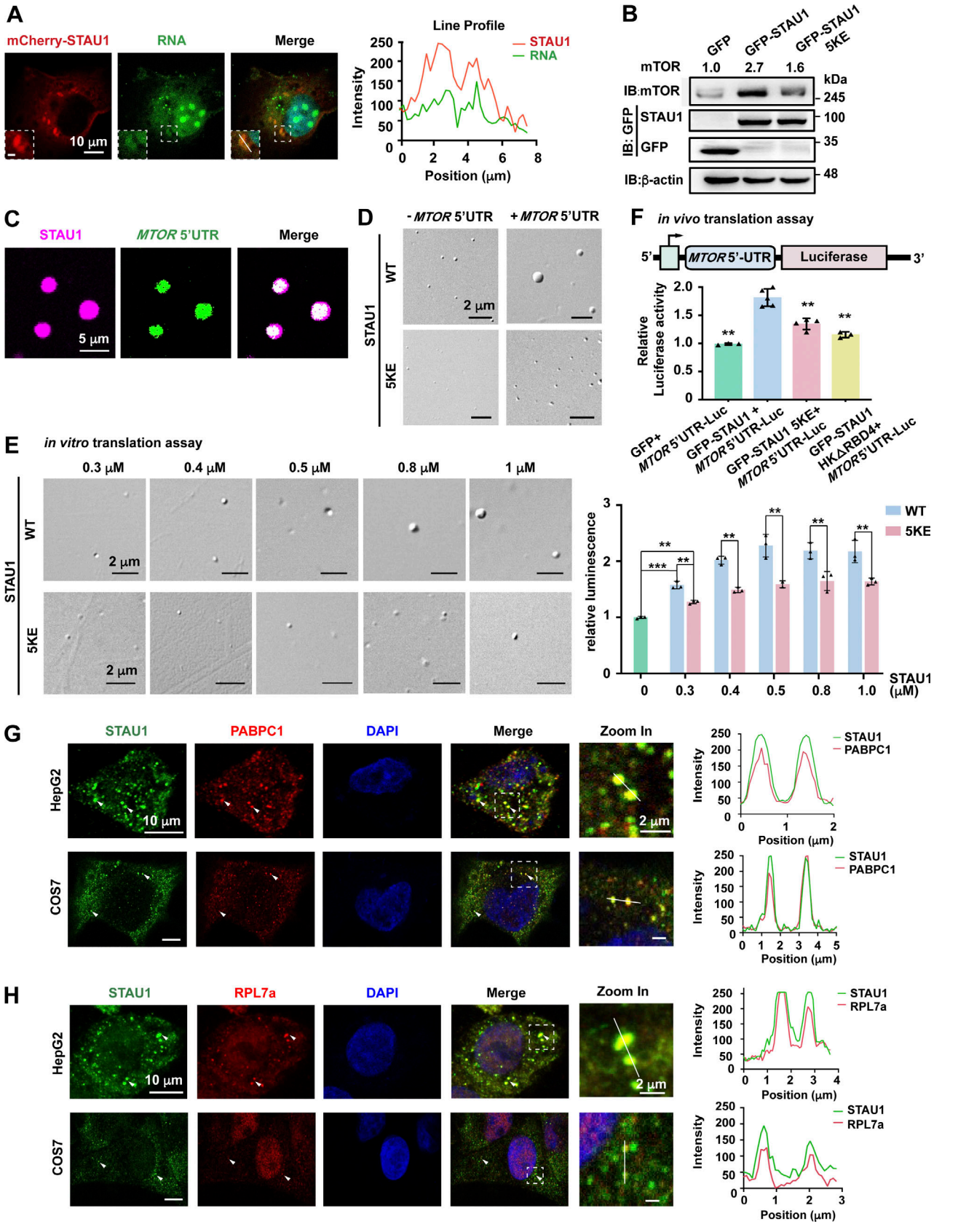

Figure 3. **Recruitment of *MTOR* RNA at its 5′UTR into STAU1 condensate promotes its translation. (A)** Left: Representative images showing co-localization of mCherry-STAU1 (red) with RNA (green) within STAU1 puncta in COS7 cells. RNA was stained with SYTO 12 Green-Fluorescent Nucleic Acid Stain. Scale bars, 10 μm; insets, 2 μm. Right: Line plot of STAU1 and RNA fluorescence intensities in indicated box regions. **(B)** Representative WB assay images

of COS7 cells exogenously expressing GFP vector, GFP-STAU1 WT, or 5KE mutant. **(C)** Representative images showing the colocalization of Cy5-STAU1 (5 µM, magenta) and *MTOR* 5′UTR (40 ng, green) stained by SYTO12 in the liquid droplets. **(D)** Representative DIC images of STAU1 WT or 5KE mutant (1 µM) with or without *MTOR* 5′UTR RNA (40 ng). Images were acquired at ∼3 min after injecting the mixture into the chamber. **(E)** Left: Representative DIC images of the reaction mixtures with STAU1 WT or 5KE mutant after the in vitro translation assay. Protein concentrations of STAU1 WT or 5KE are indicated on the top of the panel. Scale bar, 2 µm. Right: Statistical data for the relative luminescence of different samples. Statistics data are presented as the mean ± SD of triplicate experiments; $^{**}P < 0.01$, $^{***}P < 0.001$ using one-way ANOVA with Tukey's multiple comparison test. **(F)** Luciferase assay showing enhanced translation of luciferase mRNA in the presence of STAU1 WT but not the 5KE mutant. The upper panel is the schematic of *MTOR*-5′UTR-Luciferase reporter. Statistics data are presented as the mean ± SD of four independent experiments; $^{**}P < 0.01$ using one-way ANOVA with Tukey's multiple comparison test. **(G and H)** Left: Representative immunostaining images showing co-localization and enrichment (white arrows) of endogenous PABPC1 (red) (G) or RPL7a (red) (H) within STAU1 condensate (green) in HepG2 and COS7 cells. Scale bar: 10 µm; zoom in: 2 µm. Right: Fluorescence intensities of STAU1 and PABPC1 or RPL7a were quantified along a line drawn in the magnified boxes.

STAU1 condensate promotes target RNA translation

As STAU1 has been shown to enhance the translation efficiency of target mRNAs upon binding to their 5′UTRs (Dugré-Brisson et al., 2005), we next tested whether LLPS of STAU1 contributes to this process using a rabbit reticulocyte lysate in vitro translation assay and luminescence was monitored as an indicator for *MTOR*-5′UTR-Luciferase mRNA translation. The addition of an increasing amount of STAU1 to the reaction mixture gradually enhanced the translation of Luciferase mRNA (Fig. 3 E). In sharp contrast, Luciferase mRNA translation was only slightly enhanced in the presence of STAU1 5KE. The assay mixtures after reaction were then subject to DIC microscopy analysis, and larger droplets were observed in mixtures with enhanced RNA translation, indicating a high correlation of STAU1 LLPS with its ability to promote target mRNA translation (Fig. 3 E).

We next performed luciferase reporter assays in vivo to further verify the effects of STAU1 LLPS on translation. We inserted the *MTOR*-5′UTR to the upstream of Luciferase (referred to as *MTOR*-5′UTR-LUC) and cotransfected this construct with EGFP-tagged STAU1, STAU1 5KE, or control EGFP vector in COS7 cells (Fig. 3 F and Fig. S2 G). Exogenous STAU1 resulted in a significant increase of luciferase activity from *MTOR*-5′UTR-LUC construct, while the 5KE mutation exhibited a weakened promotion effect on translation, further demonstrating a positive role of STAU1 LLPS in promoting the translation of target mRNAs such as *-MTOR* mRNA. To further confirm the effect of STAU1 condensates in mRNA translation, we generated an RNA-binding-deficient STAU1 mutant based on the reported structure of STAU1 dsRBD3-4 in complex with ARF1 SBS (PDB ID: 6HTU) (Lazzaretti et al., 2018). Combinational H212,K214A mutation on RBD3 and deletion of RBD4 (referred to as HKΔRBD4 hereafter) disrupted the RNA binding capacity of STAU1 without interfering with its LLPS ability (Fig. S2, H–K). Noted that the RNA-binding-deficient STAU1 HKΔRBD4 could not promote mTOR translation both in vitro and in vivo (Fig. S2, G and L; and Fig. 3 F), suggesting that the recruitment of target RNAs into STAU1 condensate is essential for translation enhancement.

Given the role of STAU1 condensate in promoting mRNA translation, we next investigated whether STAU1 condensate could recruit translation factors and ribosomal subunits. It was observed that the translation factor poly(A) tail-binding protein C1 (PABPC1) (Passmore and Coller, 2022) and large ribosomal subunit protein L7a (RPL7a) (Hemmerich et al., 1993) were well colocalized with endogenous STAU1 puncta in both HepG2 and COS7 cells (Fig. 3, G and H), indicating that STAU1 condensate promote translation of its target mRNAs by recruiting and enriching multiple components of the translation machinery.

Elevated STAU1 LLPS enhances mTOR activity and inhibits autophagosome–lysosome fusion

STAU1 overabundance was found to be associated with hyperactive mTOR (Paul et al., 2021), a factor regulating multiple stages of the autophagic process, resulting in the inhibition of autophagy (Kim and Guan, 2015). We sought to investigate whether excessive STAU1 LLPS-mediated translational enhancement of mTOR ultimately resulted in autophagy dysfunction. To assess autophagic flux, Hela cells stably expressing the RFP-GFP-LC3 reporter were generated, in which autophagosomes were labeled with both red and green fluorescence whereas autolysosomes with only red fluorescence. Upon efficient fusion between autophagosomes and lysosomes, exposure to the low pH of the autolysosome led to a dramatic loss of acid-sensitive green fluorescence, causing a shift in fluorescence to red, thus providing a marker of autophagic flux (Fig. S3 A). Much more yellow puncta were observed in Hela cells expressing STAU1 WT than mock cells with or without the treatment of autophagy stimulator rapamycin (RAPA) (Bové et al., 2011), as well as those expressing LLPS-deficient STAU1 5KE and RNA-binding-deficient STAU1 HKΔRBD4 mutants (Fig. 4, A–C). These data suggest STAU1 overabundance causes defects in autophagosome–lysosome fusion and inhibition of autophagic flux, which is dependent on its LLPS and RNA-binding abilities.

To further demonstrate the above hypothesis, we exogenously expressed comparable amounts of GFP-STAU1 WT or 5KE mutant in SH-SY5Y cells and COS7 cells, respectively, and analyzed the levels of mTOR and related proteins by quantitative Western blotting (WB) analysis (Fig. 4 D and Fig. S3 B). Expression of STAU1 significantly increased the protein levels of mTOR, p-mTOR, as well as phosphorylation of mTOR downstream targets including eukaryotic initiation factor 4E binding protein (4E-BP) and p70 S6 kinase 1 (S6K1) (Liu and Sabatini, 2020), implying hyperactivation of mTOR pathway. Enhanced mTOR signaling then led to abnormal accumulation of autophagic markers p62 and LC3B-II, indicative of inefficient autophagosome-lysosome fusion. In sharp contrast, expression of the LLPS-deficient STAU1 5KE mutant or the RNA-binding-deficient STAU1 HKΔRBD4 mutant exhibited no observable impact on mTOR and autophagic pathways (Fig. 4 D and Fig. S3, B and C).

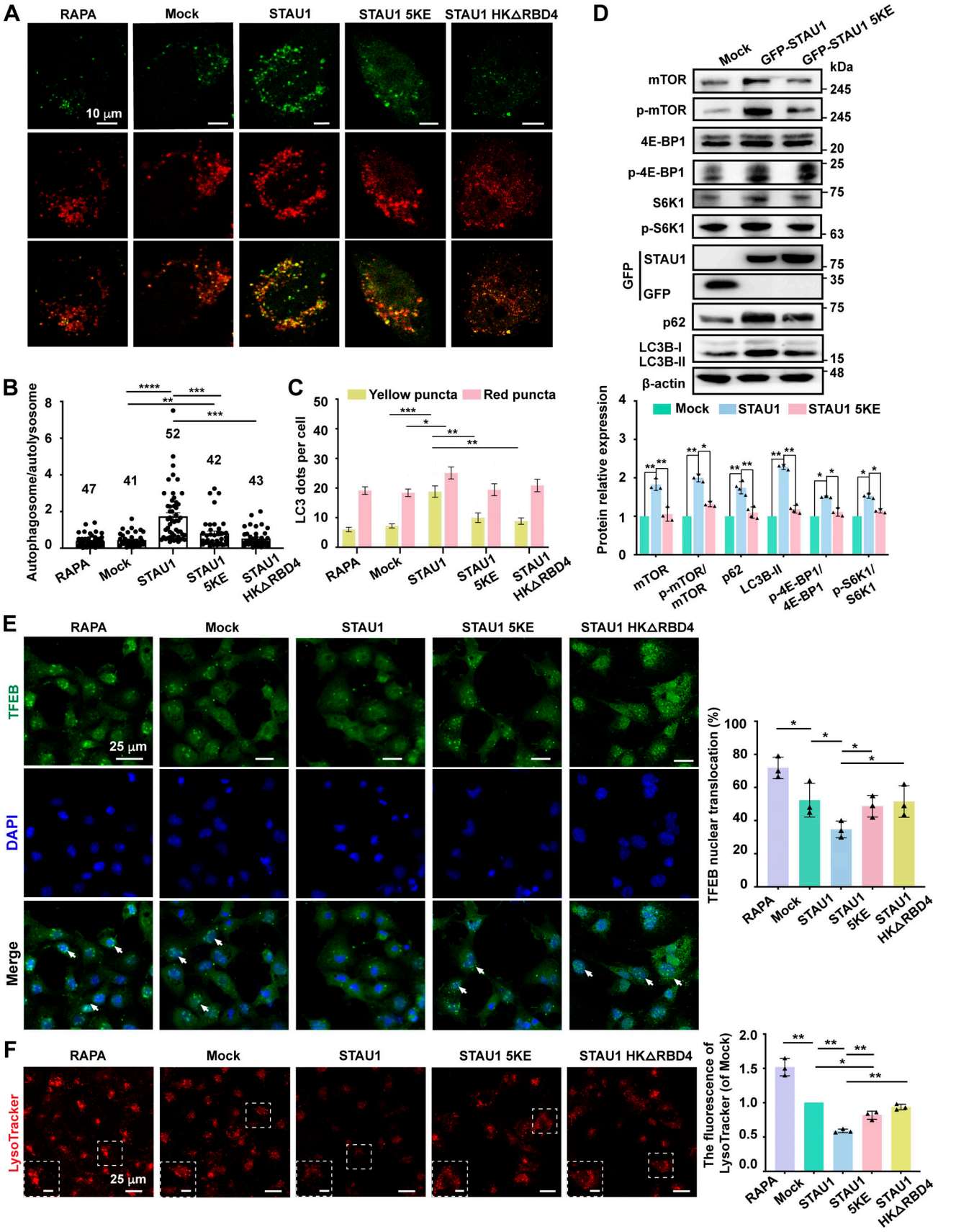

Figure 4. **STAU1 condensate enhances mTOR signaling and autophagy dysfunction. (A)** Representative images of autophagic flux measurement in Hela cells that stably expressing the mRFP-GFP-LC3 reporter and Flag (MOCK), Flag-STAU1, Flag-STAU1 5KE, or Flag-STAU1 HKΔRBD4. Untransfected Hela cells

were treated with 100 nM rapamycin as a control for effective fusion. Scale bar, 10 µm. **(B)** Quantification of the autophagosome/autolysosome ratio (red$^+$green$^+$ puncta: red$^+$ green$^-$ puncta) in A. *n*, number of individual cells (on the top of the batch). **(C)** Quantification of the LC3 dots per cell in A. Statistics data are presented as the mean ± SEM; *P < 0.05, **P < 0.01, ***P < 0.001, and ****P < 0.0001 using one-way ANOVA with Tukey's multiple comparison test. **(D)** Upper: Representative WB images of mTOR, p-mTOR, p62, 4EBP1, p-4EBP1, S6K1, p-S6K1, and LC3B-II levels in COS7 cells exogenously expressing control PEGFP-C3, GFP-STAU1 WT, or 5KE. Lower: Statistic graph of quantified fold changes. The density of each band was normalized by β-actin. The phosphoproteins were normalized to the unphosphorylated protein. Statistics data are presented as the mean ± SD of three independent experiments; **P < 0.01 using one-way ANOVA with Tukey's multiple comparison test. **(E)** Left: Representative images showing the distribution of TFEB in COS7 cells expressing PEGFP-C3, GFP-STAU1 WT, 5KE, or HKΔRBD4, as detected by immunoflurescence using TFEB antibody. Untransfected cells were treated with 100 nM rapamycin. White arrows indicate the expression of TFEB in the nucleus. Scale bar, 25 µm. Right: Quantification of the number of cells with nuclear TFEB localization. Data were collected from three independent experimental batches, with >300 cells counted for each batch. Statistics data in this figure are presented as the mean ± SD; *P < 0.05 using one-way ANOVA with Tukey's multiple comparison test. **(F)** Representative images and quantification of Lyso-Tracker Red staining in COS7 cells transfected with PEGFP-C3, GFP-STAU1 WT, 5KE, or HKΔRBD4. Scale bars, 25 µm; insets, 10 µm. >300 cells were assessed blind and quantified for each batch. Statistics data are presented as the mean ± SD of three independent experiments; *P < 0.05, **P < 0.01 using one-way ANOVA with Tukey's multiple comparison test.

We further showed that STAU1-overexpressed cells treated with bafilomycin A1 (BafA1, an inhibitor of autophagosome–lysosome fusion) did not further increase LC3-II and p62 levels (Fig. S3 D), demonstrating that STAU1 was indeed involved in inhibiting autophagosome–lysosome fusion. An increase in STAU1 level upon BafA1 treatment was observed (Fig. S3 D), suggesting inefficient STAU1 clearance by autophagy. Then we wondered whether STAU1 condensates could be recognized by the autophagy degradation system, thus competing for the clearance machinery with other biomolecular condensates or aggregates (e.g., HTT Q111 aggregates in HD STHdh$^{Q111/Q111}$ cells; Fig. 1 D). We found that STAU1 condensate could not recruit LC3B, p62, and ubiquitin with or without BafA1 treatment (Fig. S3, E–G), implying that the formation of STAU1 condensate was independent of autophagy factors, and the fraction of STAU1 degraded by autophagy was not in the condensed form.

STAU1 condensate impaired TFEB nuclear translocation and lysosomal acidification

TFEB (transcription factor EB) is a master regulator of autophagy and lysosomal function by driving the expression of genes belonging to the Coordinated Lysosomal Expression and Regulation (CLEAR) network (Sardiello et al., 2009; Settembre et al., 2011). Inhibition of mTOR activates TFEB by promoting its nuclear translocation, thus leading to the activation of its target genes required for lysosome biogenesis, autophagosome–lysosome fusion, and lysosome function (Martina et al., 2012; Settembre et al., 2011). We, therefore, tested whether elevation of STAU1 LLPS could impair TFEB nuclear translocation to repress target gene transcription. In line with our hypothesis, STAU1 overexpression reduced the percentage of cells showing the nuclear distribution of endogenous TFEB in COS7 cells (Fig. 4 E). In contrast, cells transfected with STAU1 5KE or HKΔRBD4 mutant exhibit enhanced accumulation of TFEB in the nucleus. Similarly, coexpression of GFP-TFEB with mCherry-STAU1 WT but not the 5KE or HKΔRBD4 mutant efficiently inhibited the nuclear translocation of GFP-TFEB (Fig. S4 A). We further precluded the possibility that cytoplasmic STAU1 condensates recruited TFEB to inhibit its nuclear translocation (Fig. S4, B and C).

Consistent with the above results, mass spectrometry data analysis revealed that in U251 cells overexpressing STAU1, several downstream target genes of TFEB were downregulated, including subunits of the vacuolar ATPase (v-ATPase) (Fig. S4 D), which are essential for lysosome acidification (Wang et al., 2024). We next used the fluorescence intensities of LysoTracker (Hu et al., 2022) and LysoSensor (Li et al., 2015) to indicate the degree of lysosomal acidification. Overexpression of STAU1 WT but not the 5KE or HKΔRBD4 mutant significantly decreased the fluorescence intensity of LysoTracker- or LysoSensor-labeled lysosomes (Fig. 4 F and Fig. S4 E), indicating that elevated STAU1 LLPS impaired lysosomal acidification.

In summary, these data demonstrate that STAU1 overabundance-induced excessive formation of STAU1 condensate and the subsequent hyperactivation of mTOR signaling impair lysosomal function and autophagic pathway.

STAU1 condensate suppresses the autophagic process in mouse HD cells

We have observed significantly enhanced STAU1 LLPS in mouse HD striatal STHdh$^{Q111/Q111}$ cells, accompanied by elevation of mTOR level (Fig. 1 D). We wondered whether excessive STAU1 condensates would result in autophagy dysfunction in STHdh$^{Q111/Q111}$ cells. To test this hypothesis, we first knocked down STAU1 in the mouse HD STHdh$^{Q111/Q111}$ cells with two different shRNAs, and the STAU1 expression levels were considerably downregulated by sh-mSTAU1-1 (Fig. S4 F), which was then used for depleting mSTAU2 in the subsequent experiments. When expressing RFP-GFP-LC3B, more yellow puncta were observed in HD cells (STHdh$^{Q111/Q111}$) compared with the WT cells (STHdh$^{Q7/Q7}$), indicating the dysfunction of autophagy (Fig. 5 A). Compared with WT cells, levels of STAU1, mTOR, and p-mTOR were significantly increased in HD ones, along with an obvious accumulation of p-4E-BP1, p-S6K1, p62, and LC3B-II (Fig. 5 B). As expected, depletion of STAU1 in HD STHdh$^{Q111/Q111}$ cells reduced the protein levels of mTOR, p62, and LC3B-II, as well as phosphorylation levels of mTOR, 4E-BP1, and S6K1 to normal state, and the autophagosome/autolysosome ratio was dramatically decreased compared with that in HD cells (Fig. 5, A and B). In addition, impaired TFEB nuclear translocation was observed in HD cells (STHdh$^{Q111/Q111}$) when compared with WT cells (STHdh$^{Q7/Q7}$), while depletion of STAU1 promoted the nuclear translocation of endogenous TFEB in HD STHdh$^{Q111/Q111}$ cells (Fig. 5, C and D). We also found that lysosomal acidification could be restored in STAU1-KD STHdh$^{Q111/Q111}$ cells (Fig. 5 E).

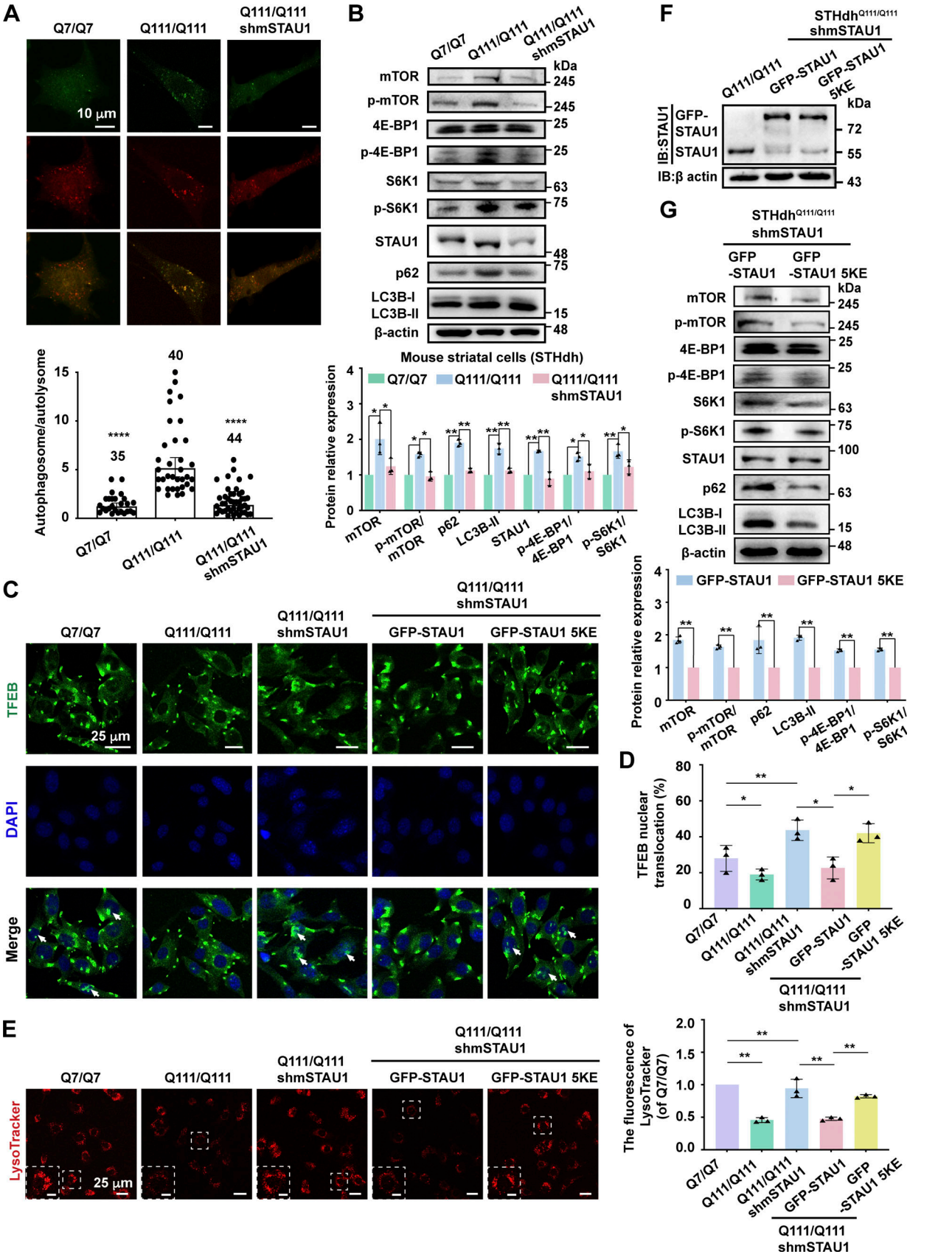

Figure 5. **STAU1 LLPS enhances mTOR signaling and impairs autophagy flux in HD cell line. (A)** Upper: Representative images of autophagic flux measurement in STHdh cells expressing the mRFP-GFP-LC3 reporter. Scale bar, 10 μm. Lower: Statistic graph of mRFP-GFP-LC3 tandem assay showing an

increased autophagosome/autolysosome ratio in STHdh$^{Q111/Q111}$ cells compared with STHdh$^{Q7/Q7}$ cells, indicating low autophagic flux. STAU1 depletion resulted in a decreased autophagosome/autolysosome ratio in STHdh$^{Q111/Q111}$ cells. *n*, number of individual cells (on the top of the batch). Statistics data are presented as the mean ± SEM; ****P < 0.0001 using one-way ANOVA with Tukey's multiple comparison test. **(B)** Upper: Representative WB images showing HD cell line (STHdh$^{Q111/Q111}$) is autophagy-defective compared to WT cells (STHdh$^{Q7/Q7}$) and STAU1 depletion lowers protein levels of mTOR and other autophagy pathway proteins. Lower: Statistic graph of quantified fold changes. **(C)** Representative immunofluorescence images showing the distribution of TFEB in WT (STHdh$^{Q7/Q7}$), HD (STHdh$^{Q111/Q111}$), STHdh$^{Q111/Q111}$-STAU1-KD, and DOX-induced STHdh$^{Q111/Q111}$-STAU1-KD/GFP-STAU1 or GFP-STAU1 5KE cells. White arrows indicate the expression of TFEB in the nucleus. Scale bar, 25 µm. **(D)** Quantification of the number of cells with nuclear TFEB localization in C. Data were collected from three independent experimental batches, with >300 cells counted for each batch. **(E)** Representative images and quantification of Lyso-Tracker Red staining in WT (STHdh$^{Q7/Q7}$), HD (STHdh$^{Q111/Q111}$), STHdh$^{Q111/Q111}$-STAU1-KD, and DOX-induced STHdh$^{Q111/Q111}$-STAU1-KD/GFP-STAU1 or GFP-STAU1 5KE cells. Scale bar, 25 µm; insets, 10 µm. >300 cells were assessed blind and quantified. **(F)** Representative WB images of STAU1 expression levels in STHdh$^{Q111/Q111}$ cells, DOX-induced STHdh$^{Q111/Q111}$-STAU1-KD/GFP-STAU1 cells, and DOX-induced STHdh$^{Q111/Q111}$-STAU1-KD/GFP-STAU1 5KE cells. **(G)** Upper: Representative WB images of mTOR, p-mTOR, 4EBP1, p-4EBP, S6K1, p-S6K1, p62, and LC3-II levels in STHdh$^{Q111/Q111}$-STAU1-KD cells that stably expressing GFP-STAU1 or GFP-STAU1 5KE. Lower: Statistic graph of quantified fold changes. All statistical data in this figure except for A represent the results from three independent batches of experiments and are presented as mean ± SD; *P < 0.05, **P < 0.01 using one-way ANOVA with Tukey's multiple comparison test. Source data are available for this figure: SourceData F5.

These data further confirm the role of STAU1 in regulating autophagy.

To validate the involvement of STAU1 phase separation in this process, STAU1-KD STHdh$^{Q111/Q111}$ cells stably expressing GFP-STAU1 WT or the LLPS deficient 5KE mutant were generated, and exogenously expressed STAU1 levels were controlled to be comparable with the endogenous STAU1 by Doxycycline (DOX) induction (Fig. 5 F). Notably, protein levels of mTOR, p-mTOR, p-4E-BP1, p-S6K1, p62, and LC3B-II were significantly increased in STAU1-KD STHdh$^{Q111/Q111}$ cells expressing GFP-STAU1 WT but not the 5KE mutant (Fig. 5 G). Moreover, STAU1-KD STHdh$^{Q111/Q111}$ cells expressing GFP-STAU1 WT but not the 5KE mutant showed impaired TFEB nuclear translocation and lysosomal acidification (Fig. 5, C–E).

Taken together, STAU1 overabundance–induced excessive condensate formation in mouse HD striatal cells could lead to enhanced mTOR signaling and autophagy dysfunction, while disturbance of STAU1 condensate might be a potential strategy to lower the abnormal mTOR activity and restore autophagic pathway.

Inhibition of STAU1 LLPS ameliorates HTT aggregation in the cellular HD model

A common feature of neurodegenerative diseases is the severe accumulation of pathogenic and aggregate-prone mutant proteins due to insufficient aggregated protein clearance at least in part by autophagy. Since overabundance of STAU1 aggravates its LLPS-mediated hyperactivation of mTOR signaling and autophagy dysfunction in neurodegenerative diseases, it is of considerable interest to find out if this situation induced by high-level STAU1 could be improved by modulating the phase separation property of STAU1. To test this hypothesis, two distinct cell lines (human glioma U251 cells and African green monkey kidney COS7 cells) were overexpressed with exon 1 of HTT that contained 72 glutamine (Q) residues fused with mCherry (mCherry-HTTexon1-Q72) to model HD (Mangiarini et al., 1996). Cells overexpressing mCherry-HTTexon1-Q25 (modeling the WT state with repeats of CAG < 35) were used as a control where no obvious aggregation was observed (Fig. S5 A). Consistent with previous reports (Latoszek et al., 2022; Williams et al., 2008), exogenously expressed mCherry-HTT Q72 formed aggregates within U251 and COS7 cells (Fig. 6 A and Fig. S5 B). Treatment with rapamycin, an autophagy enhancer via inhibiting mTOR, diminished the number of cells containing aggregated proteins and decreased the sizes of aggregates (Fig. 6, A–C and Fig. S5, B–D). Notably, coexpression of GFP-STAU1 with mCherry-HTTexon1-Q72 led to a significant increase in the population of cells containing HTT Q72 aggregates and the sizes of aggregates; rapamycin treatment dramatically decreased the sizes of HTT Q72 aggregates, nevertheless, the percentage of aggregate-containing cells remained relatively high (Fig. 6, A–C and Fig. S5, B–D). However, in sharp contrast with STAU1 WT, coexpression of the LLPS-deficient STAU1 5KE mutant or RNA-binding deficient STAU1 HKΔRBD4 mutant with HTT Q72 did not aggravate the formation of HTT aggregates even in the absence of rapamycin treatment. As LLPS is concentration dependent, we wondered whether higher protein levels of STAU1 would further promote HTT Q72 aggregation. It was found that when the total amount of intracellular STAU1 was higher than twofolds of that of endogenous STAU1 (>0.8 µg GFP-STAU1 was transfected), the proportion of cells with HTT Q72 aggregates would reach a saturation value, though the sizes of aggregates slightly increased. Notably, expression of STAU1 5KE mutant did not cause obvious promotion of HTT Q72 aggregation (Fig. S5, E–H).

Protein levels of mCherry-HTT Q72 in the above U251/COS7 HD cells were analyzed by Western blot. In line with the imaging data, when GFP-STAU1 was coexpressed, a significant increase in HTT-72Q protein level was detected, whereas the protein level of HTT-72Q returned to normal in cells overexpressing STAU1 5KE mutant (Fig. 6, D and E; and Fig. S5, I and J). Rapamycin treatment decreased HTT 72Q level to a certain extent in cells coexpressing GFP-STAU1. All these data suggest a positive role of STAU1 in promoting HTT 72Q aggregation at least partially via inhibiting autophagy, and disturbing the phase separation ability of STAU1 might be a strategy to mitigate pathological HTT 72Q aggregation.

Inhibition of STAU1 LLPS ameliorates FUS/Synphilin-1 aggregation in the cellular ALS/PD model

To further verify the effect of STAU1 LLPS on autophagy dysfunction, we sought to test whether similar mechanisms were involved in other neurodegenerative disorders, such as ALS and PD. ALS is a fatal neurodegenerative disease pathologically

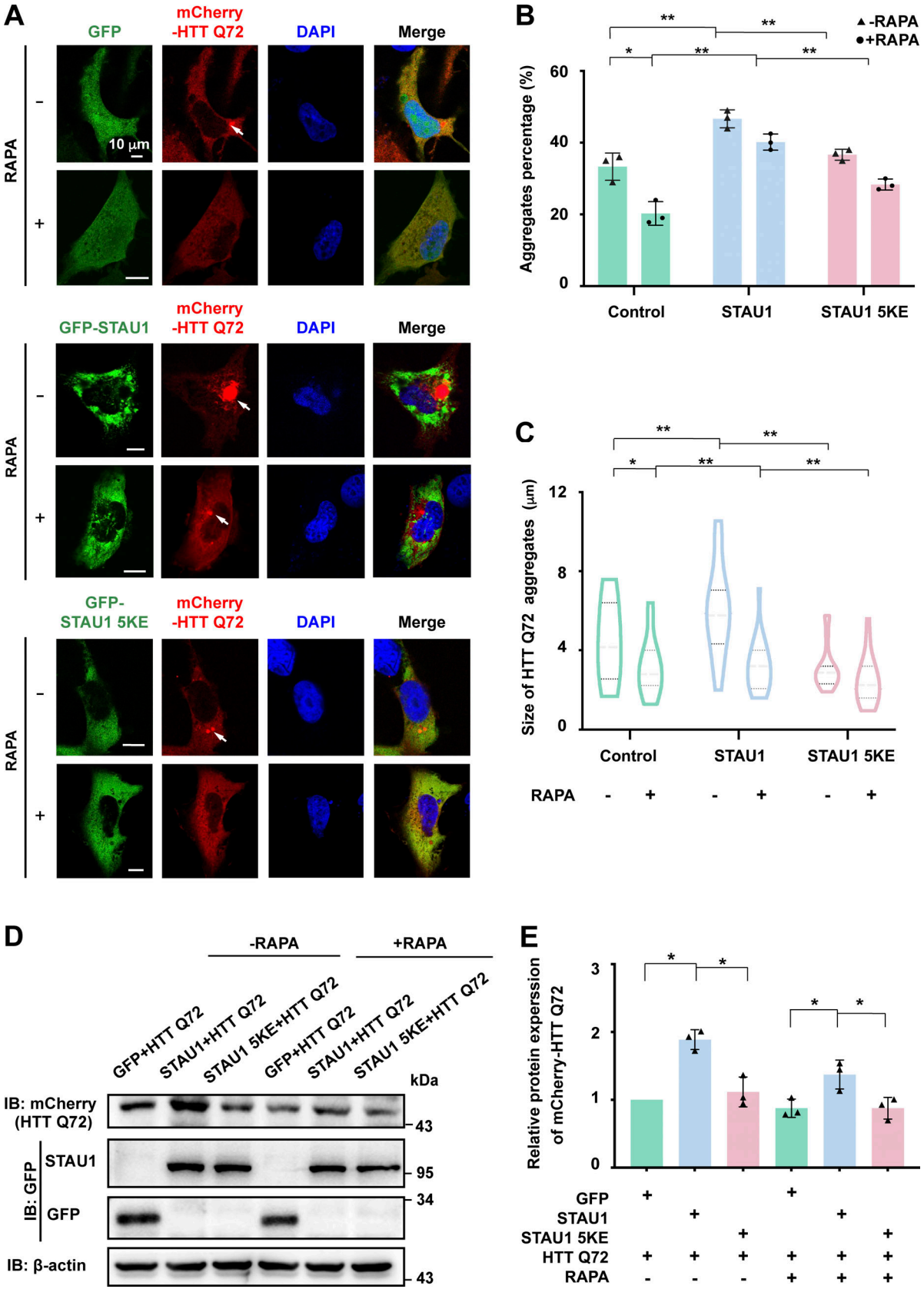

Figure 6. **LLPS of STAU1 promotes mutant HTT aggregation in the cellular HD model. (A–C)** Representative confocal images showing coexpression of mCherry-HTTexon1 Q72 with control PEGFP-C3, EGFP-STAU1 WT, or 5KE mutant in U251 cells. The mCherry-HTTexon1 Q72 transfected cells were treated with 1 μmol/l rapamycin to stimulate autophagy. Statistical data for the population of cells containing HTT Q72 aggregates or the sizes of HTT Q72 aggregates

are presented in B and C, respectively. Data were collected from three independent experimental cell culture batches, with >200 cells counted for each batch. **(D and E)** Representative WB images of HTT Q72 in U251 cells coexpressing mCherry-HTTexon1 Q72 and control GFP-vector, EGFP-STAU1 WT, or 5KE mutant. **(E)** Quantification of WB bands in D for the indicated proteins using β-actin abundance for normalization and presented as fold changes. Statistics data were collected from triplicate experiments. All statistic data are presented as mean ± SD; *P < 0.05, **P < 0.01 using one-way ANOVA with Tukey's multiple comparison test. Source data are available for this figure: SourceData F6.

characterized by degeneration of motor neurons in the brain and spinal cord (Hardiman et al., 2017). One genetic cause of ALS is the mutation of the fused in sarcoma (FUS) gene, in which the P525L mutation causes ALS cases with earlier disease onset and more aggressive progression (Kwiatkowski et al., 2009). The FUS P525L mutant protein mislocalized from the nucleus to the cytoplasm and formed large inclusions.

COS7 cells overexpressing FUS P525L were used as the cellular ALS model. In line with previous results, exogenously expressed GFP-FUS P525L robustly formed aggregates in the cytoplasm, a substantial of which could be eliminated via rapamycin-induced activation of autophagy (Fig. 7, A–C). When GFP-FUS P525L and mCherry-STAU1 were co-expressed, both the percentage of cells forming FUS aggregates and the size of FUS aggregates increased, and this phenotype could be significantly relieved with rapamycin treatment. In contrast, cells cotransfected with GFP-FUS P525L and mCherry-STAU1 5KE or mCherry-STAU1 HKΔRBD4 displayed much fewer and smaller-sized aggregates even without RAP treatment, similar to the control cells only expressing GFP-FUS P525L (Fig. 7, A–C). Consistently, coexpression of STAU1 but not the 5KE mutant led to a marked elevation of GFP-FUS P525L protein levels (Fig. 7, D and E).

PD is a neurodegenerative disorder caused by a selective loss of dopaminergic neurons and is associated with both motor and nonmotor defects (Kalia and Lang, 2016). A major hallmark of PD is the presence of intracellular protein deposits called Lewy bodies in the dying neurons, which contain different proteins, including aggregated α-Synuclein and its interacting protein Synphilin-1 (encoded by the gene *SNCAIP*) (Shirakashi et al., 2006). Overexpression of mCherry-Synphilin-1 in COS7 cells leads to the generation of cytoplasmic aggregates resembling Lewy bodies in PD (Fig. 7 F). Consistent with the above results, cotransfection of GFP-STAU1 but not the 5KE mutant or HKΔRBD4 mutant led to an increased propensity to form larger Synphilin-1 inclusions, with an upregulated Synphilin-1 protein level (Fig. 7, F–J).

Taken together, these results establish the robust correlation of overabundant STAU1 with mTOR hyperactivation and autophagy dysfunction via phase separation. Notably, targeting STAU1 LLPS might be a potential strategy to mitigate aberrant aggregation of toxic proteins such as HTT polyQ mutant, FUS P525L, and Synphilin-1 by restoring functional autophagy–lysosome pathway.

Discussion

Since autophagy plays a fundamental role in maintaining cellular homeostasis, its suppression causes deleterious consequences in diverse cellular events. Upregulation of STAU1 levels in patients with different neurodegenerative diseases was found to be associated with autophagy dysfunction, and thus might further worsen the disease symptom (Paul et al., 2018, 2023), though the detailed molecular mechanism remains elusive. In this study, we find that STAU1 forms concentration-dependent dynamic condensate enriched with RNAs and translation factors in a variety of cell lines, thereby promoting the expression of different target proteins (e.g., mTOR) at a basal level. However, pathologic elevation of STAU1 protein level and subsequent STAU1 LLPS will lead to excessive translation of target mRNAs, causing an imbalance of related cellular events including autophagy. Abnormal autophagy in turn aggravates STAU1 overabundance in neurodegenerative diseases, thereby promoting phase separation and further inhibition of autophagy. Autophagy defects affect the clearance of toxic proteins and consequently result in further accumulation of these pathological aggregates (Fig. 8). Though mounting evidence has demonstrated that the transition from a physiological liquid phase to a pathological solid phase may cause abnormal protein aggregation related to the onset and progression of various human diseases, including neurodegenerative disorders (Alberti and Hyman, 2021; Ross and Poirier, 2004), this study provides a case that excessive LLPS could exacerbate the aberrant phase separation/transition processes of these toxic proteins. Moreover, the finding that the LLPS-deficient 5KE mutation could efficiently reduce STAU1-induced abnormal accumulation of pathological protein aggregates (Figs. 6 and 7; and S5) provides a new insight for the treatment of STAU1 overabundance-related neurodegenerative disorders. On the other hand, although the RNA-binding-deficient STAU1 HKΔRBD4 mutant possessed the LLPS ability, its failure to recruit and enrich target RNA resulted in a negligible impact on mTOR signaling and autophagy pathway, suggesting that both the LLPS and RNA-binding properties of STAU1 are required for its function in regulating RNA translation. Notably, small molecules that could specifically modulate biomolecular condensates have drawn great attention as therapeutics for neurodegenerative diseases and cancers (Richard et al., 2019, *Preprint*; Wang et al., 2023). In addition to the canonical strategies to downregulate STAU1 levels by targeting STAU1 with antisense oligonucleotides (ASO) or miRNA viral vectors, designing small molecules that specifically interfere with STAU1 LLPS could be an alternative strategy to weaken the overtranslation of *MTOR* mRNA in the STAU1 condensate, thereby suppressing mTOR hyperactivation and autophagy dysfunction.

The mechanistic connection between STAU1 LLPS and autophagy seems much more intricate as mTOR signaling might not be the only pathway involved. In our cellular HD/ALS/HD models, though LLPS-deficient STAU1 5KE mutation could efficiently impair STAU1-induced severe aggregation

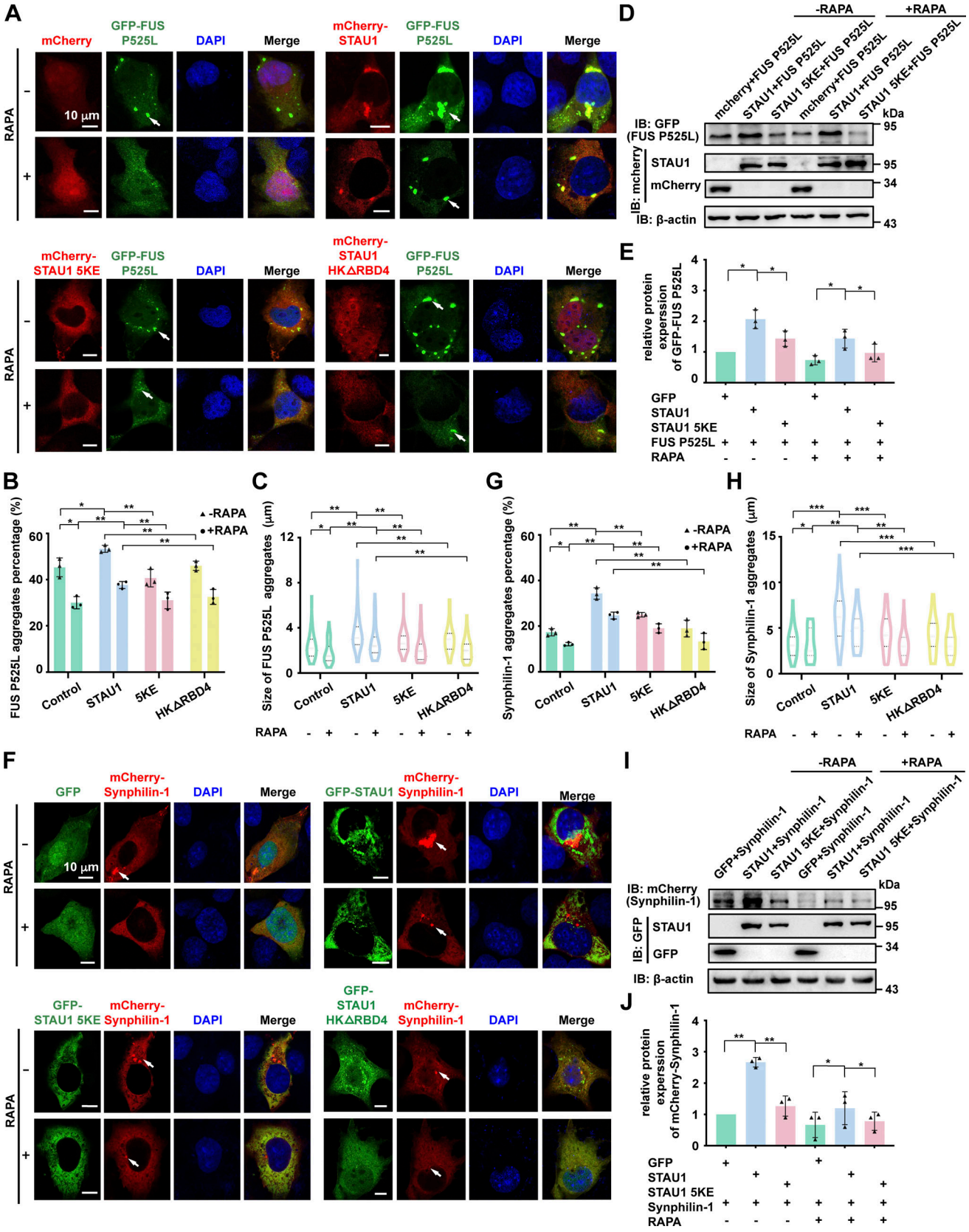

Figure 7. **LLPS of STAU1 promotes aggregation of mutant FUS/SNCAIP in the cellular ALS/PD model. (A–C)** Representative confocal images showing co-expression of EGFP-FUS P525L with control pmCherry-C1, mCherry-STAU1 WT, 5KE mutant or HKΔRBD4 mutant in COS7 cells. The EGFP-FUS P525L transfected cells were treated with 1 μmol/l rapamycin to stimulate autophagy. Statistical data for the population of cells containing FUS P525L aggregates or the sizes of FUS P525L aggregates are presented in B and C, respectively. Data were collected from three independent experimental cell culture batches, with

>200 cells counted for each batch. **(D–E)** Representative WB images of FUS P525L in COS7 cells co-expressing EGFP-FUS P525L with control pmCherry-C1, mCherry-STAU1 WT, or 5KE. **(E)** Quantification of WB bands in D. The indicated proteins were normalized using β-actin abundance and presented as fold changes. Statistics data were collected from triplicate experiments. **(F–H)** Representative confocal images of COS7 cells cotransfected with mCherry-Synphilin-1 and control PEGFP-C3, EGFP-STAU1 WT, 5KE mutant, or HKΔRBD4 mutant. The mCherry-Synphilin-1 transfected cells were treated with 1 μmol/l rapamycin to stimulate autophagy. Statistical data for the population of cells containing SNCAIP aggregates or the sizes of SNCAIP aggregates are presented in G and H, respectively. Data were collected from three independent experimental cell culture batches, with >200 cells counted for each batch. **(I and J)** Representative WB images of SNCAIP in COS7 cells co-expressing mCherry-Synphilin-1 with control PEGFP-C3, EGFP-STAU1 WT, or 5KE mutant. **(J)** Quantification of WB bands in I. Statistical data were collected from triplicate experiments. All specimens' statistics are presented as mean ± SD; *P < 0.05, **P < 0.01, ***P < 0.001 using one-way ANOVA with Tukey's multiple comparison test. Source data are available for this figure: SourceData F7.

and accumulation of pathological proteins, rapamycin treatment in cells co-expressing STAU1 WT seems not that effective (Figs. 6, 7, and S5), indicating that STAU1 condensate might promote enhanced translation of other target mRNAs that contribute to pathological protein aggregation in an mTOR independent manner. Several autophagic factors have been found to undergo LLPS and transition to control autophagic degradation of protein aggregates (Zhang, 2022). Other factor(s) regulated by STAU1 condensate might act parallel to the mTOR singling pathway in regulating aberrant protein accumulations. On the other hand, as a multifunctional posttranscriptional regulator, STAU1 also controls the stability and thus functions of diverse genes via SMD-induced RNA decay (Kim et al., 2005). In SCA2 fibroblasts, aberrant STAU1 abundance was accompanied by reduced *PCP2* mRNA as the 3′UTR of *PCP2* mRNA was recognized by STAU1 for SMD (Paul et al., 2018). In our study, more than 259 proteins have been found to be downregulated upon STAU1 overexpression (Table S2). It is plausible that by binding to the 3′-UTR of another subset of target mRNAs positively or negatively associated with the autophagy pathway, STAU1 condensate may accelerate their degradation, resulting in a more intricate control of cellular autophagy activity and pathological protein aggregation.

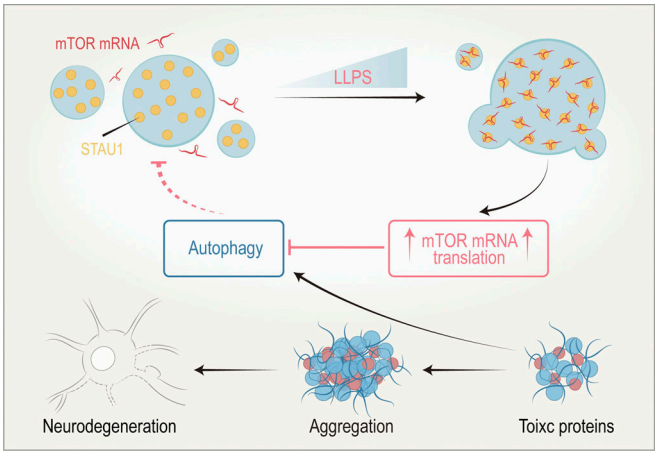

Figure 8. **Model of STAU1 condensate in neurodegeneration.** STAU1 undergoes autonomous liquid–liquid phase separation (LLPS) mainly driven by electrostatic interactions. STAU1 condensate could recruit and enrich mTOR mRNA, which further promotes STAU1 LLPS. Enhanced STAU1 LLPS promotes elevated translation of mTOR mRNA and hyperactivation of mTOR signaling. Upregulation of mTOR activity inhibits autophagy, which is the major way to degrade abnormal toxic proteins in neurodegenerative diseases. Autophagy is also responsible for the degradation of STAU1 protein. Impaired autophagy may lead to aberrant protein aggregation and STAU1 accumulation, thereby exacerbating neurodegeneration.

Materials and methods

Protein expression and purification

Various human STAU1 plasmids (Uniprot ID: O95793, RRID: SCR_002380) were individually cloned into a modified version of pET32a vector (Shan et al., 2018) (62310; Addgene). All the mutations were generated using the standard PCR-based mutagenesis method and confirmed by DNA sequencing. Recombinant proteins were expressed in *Escherichia coli* Rosetta host cells in LB medium, and *E. coli* were cultured with OD600 around 0.6–0.8 and induced with IPTG at 16°C overnight. Next, proteins were purified using a Ni^{2+}-NTA agarose affinity column followed by SEC (using HiLoad 26/600 superdex 75/200 pg columns on an AKTA Fast Protein Liquid Chromatography system; GE Healthcare) with buffer A containing 50 mM Tris (pH 8.0), 500 mM NaCl, 1 mM EDTA, and 1 mM β-mercaptoethanol (β-ME).

In vitro phase transition assay

For the in vitro LLPS assay, various recombinant STAU1 fragments prepared in buffer A were precleared via high-speed centrifugation for 10 min and concentrated at final concentrations spanning from 0.5 to 25 μM. Formations of protein condensates were monitored either directly by imaging-based methods or by sedimentation-based methods.

For imaging, proteins were injected into a homemade flow chamber comprised of a glass slide sandwiched by a coverslip with one layer of double-sided tape as a spacer for DIC (OLYMPUS IX73) or fluorescent imaging (Leica TCS SP8) (Shan et al., 2018). For the sedimentation assay, samples were subjected to centrifugation at 21,130 × *g* for 10 min. The supernatant was isolated from the pellet into a clean tube immediately after centrifugation. The pellet fraction was washed once with buffer A and thoroughly resuspended with the same buffer to the equal volume as the supernatant fraction. Proteins from both fractions were detected by 12% SDS–PAGE with Coomassie blue staining. Band intensities were quantified using the Adobe Photoshop software (RRID:SCR_014199).

For fluorescence imaging assay, STAU1 was purified in a buffer containing 100 mM $NaHCO_3$ (pH 8.3), 500 mM NaCl, 1 mM EDTA, and 1 mM β-ME. Cy5 NHS ester (AAT Bioquest) was incubated with STAU1 at room temperature for 1 h (fluorophore to protein molar ratio was 1:1). Reaction was quenched by 200 mM Tris (pH 8.0). Chemical-labeled proteins were further

purified into buffer A by Hitrap desalting column. SYTO 12 green-fluorescent nucleic acid stains (Life technologies) were added to *MTOR* 5′UTR RNA. In an inflow chamber at room temperature, the mixture of STAU1 (5 μM, with Cy5-labeled STAU1 mixed with 100 M ratios of unlabeled proteins) was observed using Leica TCS SP8.

In vitro translation assay and luciferase reporter assay

MTOR 5′UTR or *OSKAR* 3′UTR RNA was commercially synthesized in vector PUC57 and linearized by EcoRI/hindIII, and then *MTOR* 5′UTR-, *OSKAR* 3′UTR-, or *MTOR* 5′UTR-Luciferase sequence was transcribed by using RiboMAX Large Scale RNA Production Systems-SP6 and T7 (Promega). For the in vitro translation assay, *MTOR* 5′UTR-luciferase mRNA (Promega) was translated using a nuclease-treated Rabbit Reticulocyte Lysate System (Promega). Reactions were carried out according to manufacturer protocol with slight modifications. Luminescence was detected using a Synergy 2 Multi-Mode Microplate Reader (Biotech) at 25°C.

For the in vivo translation assay, *MTOR* 5′UTR sequence was inserted into Luc expression vector psi-check2 (Promega) (Addgene_97155) to obtain a recombinant vector. COS7 cells were cotransfected with the *MTOR*-5′UTR-LUC reporter and EGFP-STAU1 WT or 5KE mutant or HKΔRBD4 mutant or empty vector. The luciferase activity was detected at 48 h after transfection by Dual-Luciferase reporter assay kit (Beyotime) using a Synergy 2 Multi-Mode Microplate Reader (Biotech) at 25°C. Luciferase expression was normalized to Renilla luciferase (RLU).

Cell culture and transfection

COS7 cells (RRID: CVCL_0224), SH-SY5Y cells (RRID: CVCL_0019), and U251 cells (RRID: CVCL_0021) were from American Type Culture Collection, grown in Dulbecco's modified Eagle medium (Hyclone) containing 10% fetal bovine serum (FBS; Hyclone). STHdh$^{Q7/Q7}$ and STHdh$^{Q111/Q111}$ cells were gifts from Boxun Lu (Li et al., 2015; Yu et al., 2017). DNA transfections were performed using a polyethylenimine transfection reagent (Polysciences). 36 h after transfection, cells were used for imaging or harvested, and total protein lysate was prepared as described below.

For autophagy flux assay, Hela cells were stably transfected with mRFP-GFP-LC3 plasmids, which were selected and maintained with G418 (Geneticin). Cells stably expressing mRFP-GFP-LC3 plasmid (123230; Addgene) were plated on 12-well plates, and after overnight incubation, these cells were transfected with indicated plasmids. Untransfected cells were treated with rapamycin for 24 h, and fluorescence was measured with Leica TCS SP8 confocal microscope.

COS7 cell imaging and data analysis

The methods followed were described previously (Shan et al., 2018). For each well in a six-well plate, various STAU1 plasmids were individually transfected into COS7 cells (from ATCC, RRID: CVCL_0224) using polyethylenimine transfection reagent. After 24 h, cells were fixed with 4% paraformaldehyde and mounted on glass slides for imaging using a Leica TCS SP8 confocal microscope with a 64X oil-immersion lens with DAPI staining. Confocal images were processed with ImageJ (RRID:SCR_003070). For puncta-counting assay, data were collected from three independent batches of cultures. In each batch, at least 200 fluorescence-positive cells were counted for each group of experiments. A cell with more than two obvious fluorescence puncta was counted as a puncta-positive cell. Experiments were conducted in a blinded fashion.

LysoTracker and Lysosensor staining

The LysoTracker Red staining (Beyotime) and LysoSensor Green DND-189 (Meilun) were performed to measure the presence of acid compartments (such as lysosomes). Cells were incubated with Lyso-Tracker Red (50 nM) or LysoSensor Green (1 μM) at 37°C for 30 min. Images were captured under a Leica TCS SP8 confocal microscope. The fluorescence intensity was finally measured using ImageJ software (RRID:SCR_002285). Data were collected from three independent batches of cultures. In each batch, at least 200 fluorescence-positive cells were counted for each group of experiments.

Immunofluorescence

Cells were seeded on coverslips placed in 12-well plates. After 24–36 h, cells were fixed by 4% paraformaldehyde. Afterward, the coverslips were blocked in 3% bovine serum albumin in PBS containing 0.2% Triton X-100 for 1 h at room temperature and then incubated overnight at 4°C with the following primary antibodies: STAU1 rabbit polyclonal antibody (1:200, Cat# 14225-1-AP, RRID:AB_2302744; Proteintech), LC3B rabbit monoclonal antibody (1:200, Cat# A19665, RRID:AB_2862723; ABclonal), PABPC1 Rabbit polyclonal antibody (1:200, Cat# A14872, RRID: AB_2761752; ABclonal), RPL7A Rabbit polyclonal antibody (1: 200, Cat# A14060, RRID:AB_2760916; ABclonal), and TFEB rabbit polyclonal antibody (1:200, Cat# A7311, RRID:AB_2767851; ABclonal). The slices were washed three times in PBS for 10 min each and then incubated for 1 h at room temperature with fluorescein (FITC)-conjugated Affinipure goat anti-Rabbit secondary antibody (1:500, Cat# SA00003-2, RRID: AB_2890897; Proteintech). After nuclear staining with DAPI, the slices were mounted on glass slides for imaging using a Leica TCS SP8 confocal microscope with a 64X oil-immersion lens. Fluorescence measurement was conducted with ImageJ (RRID:SCR_003070).

Quantitative real-time PCR (qRT-PCR)

Total RNA from cells was extracted using the RNA Purification Kit (EZBioscience) and quantified using a NanoDropTM 3000 Spectrophotometer (Thermo Fisher Scientific). Total RNA was reverse transcribed by using PrimerScript RTreagent Kit with gDRNA Eraser (Takara) according to the manufacturer's instructions. qRT-PCR was conducted on an ABI Real Time 7900HT cycler with PrimerScript RT-PCR Kit (Takara), and all samples were tested three times. mRNA levels of queried genes were normalized to the averaged levels of GAPDH.

STAU1 KD and generation of inducible stable cell line

A tet-on system was used for STAU1-KD STHdh$^{Q111/Q111}$ cell line to generate inducible stable cell lines. For shRNA-mediated KD

of mouse STAU1, lentiviruses were produced using vector pMKO.1 (10676; Addgene). After 3 days of viral infection, cells were treated and selected with 4 μg/ml puromycin (Meilun). WB was performed to verify the effectiveness of STAU1 knockout. For generating an inducible stable cell line, lentiviruses were produced using vector pLVX-TetOne (171123; Addgene). After 4 days viral infection, cells were treated with 1,000 ng/ml doxycycline (60204ES03; YEASEN) for 1 day to induce the expression of GFP-STAU1 or GFP-STAU1 5KE. The GFP-positive cells were sorted by flow cytometric cell sorting and were amplified for later experimental uses. The expression levels were validated by WB.

EMSA

For each EMSA reaction (total volume, 20 μl), 20 ng denatured *MTOR* 5′UTR or *OSKAR* 3′UTR RNA was incubated individually with STAU1 WT or various mutants in a binding buffer containing 20 mM Tris-HCl (pH 7.9), 1 mM DTT, 10 mM KCl, 500 mM NaCl. After incubating for 15 min on ice, protein-bound and free RNAs were separated by electrophoresis on nondenaturing 2% polyacrylamide gels running in a 0.5 × TBE buffer at 100 V at 4°C. Gels were stained by SYBR Gold (Life Technologies) and scanned by ChemiDoc XRS+ Gel Imaging System (Bio-Rad).

HTT/FUS/SNCAIP aggregate imaging in the cellular HD/ALS/PD model

COS7/U251 cells were transiently cotransfected with mCherry-HTTexon1-Q72 or mCherry-Synphilin-1 plasmids and EGFP-STAU1 WT or 5KE mutant or HKΔRBD4 mutant plasmids or control PEGFP-C3 plasmid (53757; Addgene) to model HD or PD. COS7 cells were transiently cotransfected with GFP-FUS P525L and mCherry-STAU1 WT or 5KE mutant or HKΔRBD4 mutant plasmids or control pmCherry-C1 plasmid (67898; Addgene) to model ALS and then treated with 1 μM rapamycin for 12 h to induce autophagy. Plasmid of mCherry-HTTexon1-Q72 was a gift from Boxun Lu (Li et al., 2015). GFP-FUS P525L was a gift from Cong Liu (Li et al., 2022). Data were collected from three independent batches of cultures. In each batch, at least 200 fluorescence-positive cells were counted for each group of experiments. Imaging was performed using a Leica TCS SP8 confocal microscope with a 64X oil-immersion lens. The size and number of HTT aggregates were analyzed using ImageJ software (RRID:SCR_002285; Fiji).

Immunoblotting

Cells were harvested 36 h after transfection and lysed in a buffer containing 50 mM Tris (pH 7.4), 150 mM sodium chloride, 1% Nonidet P-40, 10 mM sodium fluoride, 1 mM sodium metavanadate, 1 mM phenylmethylsulfonyl fluoride, and protease inhibitors. Each cell lysate was subjected to centrifugation at 14,000 revolutions per minute (RPM) for 20 min at 4°C. Supernatants were used for WB and then boiled for 10 min. The captured proteins were boiled in an SDS-PAGE loading buffer and subjected to SDS-PAGE. The proteins were transferred to a 0.45 μM polyvinylidene difluoride (PVDF) membrane (Millipore), which was blocked using 3% bovine serum albumin in TBST (20 mM Tris-HCl, pH 7.4, 137 mM NaCl, and 0.1% Tween-20) buffer at room temperature for 1 h; this was followed by incubation with the following antibodies: Mouse anti-GFP antibody (1:4,000, Cat# AE012, RRID:AB_2770402; ABclonal), STAU1 rabbit polyclonal antibody (1:800, Cat# 14225-1-AP, RRID:AB_2302744; Proteintech), mTOR rabbit polyclonal antibody (1:600, Cat# A11355/A11345, RRID:AB_2758522/AB_2770475; ABclonal), phospho-mTOR antibody (Ser2448; Cat# T56571, RRID:AB_2936395; Abmart), SQSTM1/p62 rabbit polyclonal antibody (1:600, A11250; ABclonal), LC3B rabbit monoclonal antibody (1:600, Cat# A19665, RRID:AB_2862723; ABclonal), p70 S6 Kinase 1 Rabbit polyclonal antibody (1:800, A16658; ABclonal), phospho-p70 S6 Kinase 1-T389 Rabbit polyclonal antibody (1:600, AP0564; ABclonal), eIF4EBP1 Rabbit monoclonal antibody (1:800, A24691; ABclonal) Phospho-eIF4EBP1-T37/46 Rabbit polyclonal antibody (1:1,000, Cat# AP0030, RRID:AB_2771074; ABclonal), ACTB monoclonal antibody (1:8,000, Cat# AC026, RRID:AB_2768234; ABclonal) at 4°C overnight. Membranes were washed three times with TBST buffer; incubated with horseradish peroxidase-conjugated goat anti-mouse antibody (1:4,000, Cat# AS003, RRID:AB_2769851; ABclonal), horseradish peroxidase-conjugated goat anti-rabbit antibody (1:4,000, Cat# AS014, RRID:AB_2769854; ABclonal), and then visualized on a LAS3000 Chemiluminescence Imaging System. The band intensities were quantified by Photoshop software analyses after the inversion of the images. Relative protein abundances were expressed as ratios to β-actin.

FRAP assay

The in vitro FRAP analysis of Cy5-labbed STAU1 (10 μM) droplets was carried out at room temperature. The 647 signal was bleached using a 647-nm laser beam with a Leica TCS SP8 confocal microscope.

COS7 cells were cultured in glass bottom dishes and transfected as described above. FRAP assay was performed on a Leica TCS SP8 confocal microscope with a 64X oil-immersion lens. Puncta with diameters ∼1.0 μm were assayed. GFP signal was bleached using a 488-nm laser beam. The fluorescence intensity difference between prebleaching and at time 0 (the time point right after photobleaching pulse) was normalized to 100%. The experimental control is to quantify fluorescence intensities of similar puncta/cytoplasm regions without photobleaching.

Quantification and statistical analysis

Statistical parameters including the definitions and exact values of *n* (e.g., number of experiments, number of cells, etc.) were reported in the figures and corresponding figure legends. Data from autophagy flux assays were expressed as mean ± SEM, and data from other cell culture assays were expressed as mean ± SD; *P < 0.05, **P < 0.01, ***P < 0.001, and ****P < 0.0001 using one-way analysis of variance (ANOVA) with Tukey's multiple comparison test. Data from in vitro phase separation sedimentation assay and FRAP assay were expressed as mean ± SD. None of the data were removed from our statistical analysis as outliers. All statistical data were conducted in GraphPad Prism v8.2.1 (RRID:SCR_002798). All figures were assembled in Adobe Illustrator (RRID:SCR_010279). All experiments related to cell cultures and imaging studies were performed in a blinded fashion.

Online supplemental material

Fig. S1 shows the distribution and expression level of endogenous STAU1, mTOR, and autophagy factors in different cell lines, in vitro phase separation of STAU1, and identification of mutations to disturb phase separation. Fig. S2 shows the effect of RNA binding capacity on STAU1 phase separation and STAU1 condensate-mediated mRNA translation. Fig. S3 shows the influence of STAU1 phase-separation defect or RNA-binding defect on autophagy, the BafA1 +/− experiment of cells overexpressing STAU1, and the subcellular localization of STAU1 and autophagy markers. Fig. S4 shows the distribution of exogenously expressed TFEB in COS7 cells expressing STAU1 WT or mutants, downregulated TFEB targets caused by STAU1 overexpression, and Lysosensor staining assay. Fig. S5 shows the effect of overexpressed STAU1 WT or mutants on HTT Q72 aggregation in COS7 cells and the correlation of HTT Q72 aggregation with STAU1 levels. Table S1 and S2 list selected upregulated and downregulated proteins in U251 cells overexpressing STAU1 WT rather than LLPS-deficient 5KE mutant identified by mass spectrometry analysis.

Data availability

The data that support the findings of this study are available from the corresponding authors upon reasonable request.

Acknowledgments

We thank Drs. Hong Zhang, Cong Liu, and Yunli Xie for the plasmids and reagents.

This study was supported by grants from the Ministry of Science and Technology of China (2019YFA0508401) and the National Natural Science Foundation of China (32370733, 82121004, 31871394).

Author contributions: R. Zhao: Data curation, Formal analysis, Investigation, Validation, Visualization, Writing—original draft, Writing—review & editing, S. Huang: Investigation, J. Li: Investigation, A. Gu: Investigation, M. Fu: Investigation, W. Hua: Resources, Supervision, Y. Mao: Resources, Supervision, Q.-Y. Lei: Writing—review & editing, B. Lu: Methodology, Resources, Supervision, Writing—review & editing, W. Wen: Conceptualization, Data curation, Funding acquisition, Project administration, Resources, Supervision, Writing—review & editing.

Disclosures: The authors declare no competing interests exist.

Submitted: 21 November 2023
Revised: 20 March 2024
Accepted: 3 May 2024

References

Alberti, S., and A.A. Hyman. 2021. Biomolecular condensates at the nexus of cellular stress, protein aggregation disease and ageing. *Nat. Rev. Mol. Cell Biol.* 22:196–213. https://doi.org/10.1038/s41580-020-00326-6

Almasi, S., and B.J. Jasmin. 2021. The multifunctional RNA-binding protein Staufen1: An emerging regulator of oncogenesis through its various roles in key cellular events. *Cell. Mol. Life Sci.* 78:7145–7160. https://doi.org/10.1007/s00018-021-03965-w

Banani, S.F., H.O. Lee, A.A. Hyman, and M.K. Rosen. 2017. Biomolecular condensates: Organizers of cellular biochemistry. *Nat. Rev. Mol. Cell Biol.* 18:285–298. https://doi.org/10.1038/nrm.2017.7

Boulay, K., M. Ghram, W. Viranaicken, V. Trépanier, S. Mollet, C. Fréchina, and L. DesGroseillers. 2014. Cell cycle-dependent regulation of the RNA-binding protein Staufen1. *Nucleic Acids Res.* 42:7867–7883. https://doi.org/10.1093/nar/gku506

Bové, J., M. Martínez-Vicente, and M. Vila. 2011. Fighting neurodegeneration with rapamycin: Mechanistic insights. *Nat. Rev. Neurosci.* 12:437–452. https://doi.org/10.1038/nrn3068

Broadus, J., S. Fuerstenberg, and C.Q. Doe. 1998. Staufen-dependent localization of prospero mRNA contributes to neuroblast daughter-cell fate. *Nature.* 391:792–795. https://doi.org/10.1038/35861

Chen, X., X. Wu, H. Wu, and M. Zhang. 2020. Phase separation at the synapse. *Nat. Neurosci.* 23:301–310. https://doi.org/10.1038/s41593-019-0579-9

Ciechanover, A., and Y.T. Kwon. 2015. Degradation of misfolded proteins in neurodegenerative diseases: Therapeutic targets and strategies. *Exp. Mol. Med.* 47:e147. https://doi.org/10.1038/emm.2014.117

de Morrée, A., C.T.J. van Velthoven, Q. Gan, J.S. Salvi, J.D.D. Klein, I. Akimenko, M. Quarta, S. Biressi, and T.A. Rando. 2017. Staufen1 inhibits MyoD translation to actively maintain muscle stem cell quiescence. *Proc. Natl. Acad. Sci. USA.* 114:E8996–E9005. https://doi.org/10.1073/pnas.1708725114

Dugré-Brisson, S., G. Elvira, K. Boulay, L. Chatel-Chaix, A.J. Mouland, and L. DesGroseillers. 2005. Interaction of Staufen1 with the 5′ end of mRNA facilitates translation of these RNAs. *Nucleic Acids Res.* 33:4797–4812. https://doi.org/10.1093/nar/gki794

Elbarbary, R.A., W. Li, B. Tian, and L.E. Maquat. 2013. STAU1 binding 3′ UTR IRAlus complements nuclear retention to protect cells from PKR-mediated translational shutdown. *Genes Dev.* 27:1495–1510. https://doi.org/10.1101/gad.220962.113

Fleming, A., M. Bourdenx, M. Fujimaki, C. Karabiyik, G.J. Krause, A. Lopez, A. Martín-Segura, C. Puri, A. Scrivo, J. Skidmore, et al. 2022. The different autophagy degradation pathways and neurodegeneration. *Neuron.* 110:935–966. https://doi.org/10.1016/j.neuron.2022.01.017

Furic, L., M. Maher-Laporte, and L. DesGroseillers. 2008. A genome-wide approach identifies distinct but overlapping subsets of cellular mRNAs associated with Staufen1- and Staufen2-containing ribonucleoprotein complexes. *RNA.* 14:324–335. https://doi.org/10.1261/rna.720308

Gandelman, M., W. Dansithong, K.P. Figueroa, S. Paul, D.R. Scoles, and S.M. Pulst. 2020. Staufen 1 amplifies proapoptotic activation of the unfolded protein response. *Cell Death Differ.* 27:2942–2951. https://doi.org/10.1038/s41418-020-0553-9

Gleghorn, M.L., C. Gong, C.L. Kielkopf, and L.E. Maquat. 2013. Staufen1 dimerizes through a conserved motif and a degenerate dsRNA-binding domain to promote mRNA decay. *Nat. Struct. Mol. Biol.* 20:515–524. https://doi.org/10.1038/nsmb.2528

Gong, C., and L.E. Maquat. 2011. lncRNAs transactivate STAU1-mediated mRNA decay by duplexing with 3′ UTRs via Alu elements. *Nature.* 470:284–288. https://doi.org/10.1038/nature09701

Hardiman, O., A. Al-Chalabi, A. Chio, E.M. Corr, G. Logroscino, W. Robberecht, P.J. Shaw, Z. Simmons, and L.H. van den Berg. 2017. Amyotrophic lateral sclerosis. *Nat. Rev. Dis. Primers.* 3:17071. https://doi.org/10.1038/nrdp.2017.71

Hemmerich, P., A. von Mikecz, F. Neumann, O. Sözeri, G. Wolff-Vorbeck, R. Zoebelein, and U. Krawinkel. 1993. Structural and functional properties of ribosomal protein L7 from humans and rodents. *Nucleic Acids Res.* 21:223–231. https://doi.org/10.1093/nar/21.2.223

Hu, M., P. Li, C. Wang, X. Feng, Q. Geng, W. Chen, M. Marthi, W. Zhang, C. Gao, W. Reid, et al. 2022. Parkinson's disease-risk protein TMEM175 is a proton-activated proton channel in lysosomes. *Cell.* 185:2292–2308.e20. https://doi.org/10.1016/j.cell.2022.05.021

Jumper, J., R. Evans, A. Pritzel, T. Green, M. Figurnov, O. Ronneberger, K. Tunyasuvunakool, R. Bates, A. Žídek, A. Potapenko, et al. 2021. Highly accurate protein structure prediction with AlphaFold. *Nature.* 596:583–589. https://doi.org/10.1038/s41586-021-03819-2

Kalia, L.V., and A.E. Lang. 2016. Parkinson disease in 2015: Evolving basic, pathological and clinical concepts in PD. *Nat. Rev. Neurol.* 12:65–66. https://doi.org/10.1038/nrneurol.2015.249

Kim, Y.C., and K.L. Guan. 2015. mTOR: a pharmacologic target for autophagy regulation. *J. Clin. Invest.* 125:25–32. https://doi.org/10.1172/JCI73939

Kim, Y.K., L. Furic, L. Desgroseillers, and L.E. Maquat. 2005. Mammalian Staufen1 recruits Upf1 to specific mRNA 3'UTRs so as to elicit mRNA decay. *Cell*. 120:195–208. https://doi.org/10.1016/j.cell.2004.11.050

Kwiatkowski, T.J. Jr., D.A. Bosco, A.L. Leclerc, E. Tamrazian, C.R. Vanderburg, C. Russ, A. Davis, J. Gilchrist, E.J. Kasarskis, T. Munsat, et al. 2009. Mutations in the FUS/TLS gene on chromosome 16 cause familial amyotrophic lateral sclerosis. *Science*. 323:1205–1208. https://doi.org/10.1126/science.1166066

Lafontaine, D.L.J., J.A. Riback, R. Bascetin, and C.P. Brangwynne. 2021. The nucleolus as a multiphase liquid condensate. *Nat. Rev. Mol. Cell Biol.* 22: 165–182. https://doi.org/10.1038/s41580-020-0272-6

Latoszek, E., M. Wiweger, J. Ludwiczak, S. Dunin-Horkawicz, J. Kuznicki, and M. Czeredys. 2022. Siah-1-interacting protein regulates mutated huntingtin protein aggregation in Huntington's disease models. *Cell Biosci.* 12:34. https://doi.org/10.1186/s13578-022-00755-0

Laver, J.D., X. Li, K. Ancevicius, J.T. Westwood, C.A. Smibert, Q.D. Morris, and H.D. Lipshitz. 2013. Genome-wide analysis of Staufen-associated mRNAs identifies secondary structures that confer target specificity. *Nucleic Acids Res.* 41:9438–9460. https://doi.org/10.1093/nar/gkt702

Lazzaretti, D., L. Bandholz-Cajamarca, C. Emmerich, K. Schaaf, C. Basquin, U. Irion, and F. Bono. 2018. The crystal structure of Staufen1 in complex with a physiological RNA sheds light on substrate selectivity. *Life Sci. Alliance*. 1:e201800187. https://doi.org/10.26508/lsa.201800187

Lebeau, G., M. Maher-Laporte, L. Topolnik, C.E. Laurent, W. Sossin, L. Desgroseillers, and J.C. Lacaille. 2008. Staufen1 regulation of protein synthesis-dependent long-term potentiation and synaptic function in hippocampal pyramidal cells. *Mol. Cell. Biol.* 28:2896–2907. https://doi.org/10.1128/MCB.01844-07

Levine, B., and G. Kroemer. 2008. Autophagy in the pathogenesis of disease. *Cell*. 132:27–42. https://doi.org/10.1016/j.cell.2007.12.018

Li, D., S. Huang, Y. Chai, R. Zhao, J. Gong, Q.C. Zhang, G. Ou, and W. Wen. 2023a. A paternal protein facilitates sperm RNA delivery to regulate zygotic development. *Sci. China Life Sci.* 66:2342–2353. https://doi.org/10.1007/s11427-022-2332-5

Li, F., J. Wang, S. Sun, H. Wang, Z. Tang, and G. Nie. 2015. Facile synthesis of pH-sensitive germanium nanocrystals with high quantum yield for intracellular acidic compartment imaging. *Small*. 11:1954–1961. https://doi.org/10.1002/smll.201402743

Li, J., K. Zhu, A. Gu, Y. Zhang, S. Huang, R. Hu, W. Hu, Q.Y. Lei, and W. Wen. 2023b. Feedback regulation of ubiquitination and phase separation of HECT E3 ligases. *Proc. Natl. Acad. Sci. USA*. 120:e2302478120. https://doi.org/10.1073/pnas.2302478120

Li, P., S. Banjade, H.C. Cheng, S. Kim, B. Chen, L. Guo, M. Llaguno, J.V. Hollingsworth, D.S. King, S.F. Banani, et al. 2012. Phase transitions in the assembly of multivalent signalling proteins. *Nature*. 483:336–340. https://doi.org/10.1038/nature10879

Li, P., X. Yang, M. Wasser, Y. Cai, and W. Chia. 1997. Inscuteable and Staufen mediate asymmetric localization and segregation of prospero RNA during Drosophila neuroblast cell divisions. *Cell*. 90:437–447. https://doi.org/10.1016/S0092-8674(00)80504-8

Li, Y., S. Lu, J. Gu, W. Xia, S. Zhang, S. Zhang, Y. Wang, C. Zhang, Y. Sun, J. Lei, et al. 2022. SARS-CoV-2 impairs the disassembly of stress granules and promotes ALS-associated amyloid aggregation. *Protein Cell*. 13: 602–614. https://doi.org/10.1007/s13238-022-00905-7

Liu, G.Y., and D.M. Sabatini. 2020. mTOR at the nexus of nutrition, growth, ageing and disease. *Nat. Rev. Mol. Cell Biol.* 21:183–203. https://doi.org/10.1038/s41580-019-0199-y

Liu, Z., Y. Yang, A. Gu, J. Xu, Y. Mao, H. Lu, W. Hu, Q.Y. Lei, Z. Li, M. Zhang, et al. 2020. Par complex cluster formation mediated by phase separation. *Nat. Commun.* 11:2266. https://doi.org/10.1038/s41467-020-16135-6

Mangiarini, L., K. Sathasivam, M. Seller, B. Cozens, A. Harper, C. Hetherington, M. Lawton, Y. Trottier, H. Lehrach, S.W. Davies, and G.P. Bates. 1996. Exon 1 of the HD gene with an expanded CAG repeat is sufficient to cause a progressive neurological phenotype in transgenic mice. *Cell*. 87:493–506. https://doi.org/10.1016/S0092-8674(00)81369-0

Martina, J.A., Y. Chen, M. Gucek, and R. Puertollano. 2012. MTORC1 functions as a transcriptional regulator of autophagy by preventing nuclear transport of TFEB. *Autophagy*. 8:903–914. https://doi.org/10.4161/auto.19653

Mayr, C., T. Mittag, T.D. Tang, W. Wen, H. Zhang, and H. Zhang. 2023. Frontiers in biomolecular condensate research. *Nat. Cell Biol.* 25: 512–514. https://doi.org/10.1038/s41556-023-01102-2

Menzies, F.M., A. Fleming, A. Caricasole, C.F. Bento, S.P. Andrews, A. Ashkenazi, J. Füllgrabe, A. Jackson, M. Jimenez Sanchez, C. Karabiyik, et al. 2017. Autophagy and neurodegeneration: Pathogenic mechanisms and therapeutic opportunities. *Neuron*. 93:1015–1034. https://doi.org/10.1016/j.neuron.2017.01.022

Micklem, D.R., J. Adams, S. Grünert, and D. St Johnston. 2000. Distinct roles of two conserved Staufen domains in oskar mRNA localization and translation. *EMBO J.* 19:1366–1377. https://doi.org/10.1093/emboj/19.6.1366

Mitsumori, K., Y. Takei, and N. Hirokawa. 2017. Components of RNA granules affect their localization and dynamics in neuronal dendrites. *Mol. Biol. Cell*. 28:1412–1417. https://doi.org/10.1091/mbc.e16-07-0497

Oh, Y., J. Park, J.I. Kim, M.Y. Chang, S.H. Lee, Y.H. Cho, and J. Hwang. 2018. Lin28B and miR-142-3p regulate neuronal differentiation by modulating Staufen1 expression. *Cell Death Differ.* 25:432–443. https://doi.org/10.1038/cdd.2017.182

Passmore, L.A., and J. Coller. 2022. Roles of mRNA poly(A) tails in regulation of eukaryotic gene expression. *Nat. Rev. Mol. Cell Biol.* 23:93–106. https://doi.org/10.1038/s41580-021-00417-y

Paul, S., W. Dansithong, K.P. Figueroa, M. Gandelman, D.R. Scoles, and S.M. Pulst. 2021. Staufen1 in human neurodegeneration. *Ann. Neurol.* 89: 1114–1128. https://doi.org/10.1002/ana.26069

Paul, S., W. Dansithong, K.P. Figueroa, D.R. Scoles, and S.M. Pulst. 2018. Staufen1 links RNA stress granules and autophagy in a model of neurodegeneration. *Nat. Commun.* 9:3648. https://doi.org/10.1038/s41467-018-06041-3

Paul, S., W. Dansithong, M. Gandelman, K.P. Figueroa, T. Zu, L.P.W. Ranum, D.R. Scoles, and S.M. Pulst. 2023. Staufen impairs autophagy in neurodegeneration. *Ann. Neurol.* 93:398–416. https://doi.org/10.1002/ana.26515

Paulson, H.L., V.G. Shakkottai, H.B. Clark, and H.T. Orr. 2017. Polyglutamine spinocerebellar ataxias - from genes to potential treatments. *Nat. Rev. Neurosci.* 18:613–626. https://doi.org/10.1038/nrn.2017.92

Querfurth, H., and H.K. Lee. 2021. Mammalian/mechanistic target of rapamycin (mTOR) complexes in neurodegeneration. *Mol. Neurodegener.* 16: 44. https://doi.org/10.1186/s13024-021-00428-5

Ramos, H., A. Monette, M. Niu, A. Barrera, B. López-Ulloa, Y. Fuentes, P. Guizar, K. Pino, L. DesGroseillers, A.J. Mouland, and M. López-Lastra. 2022. The double-stranded RNA-binding protein, Staufen1, is an IRES-transacting factor regulating HIV-1 cap-independent translation initiation. *Nucleic Acids Res.* 50:411–429. https://doi.org/10.1093/nar/gkab1188

Ravel-Chapuis, A., G. Bélanger, R.S. Yadava, M.S. Mahadevan, L. DesGroseillers, J. Côté, and B.J. Jasmin. 2012. The RNA-binding protein Staufen1 is increased in DM1 skeletal muscle and promotes alternative pre-mRNA splicing. *J. Cell Biol.* 196:699–712. https://doi.org/10.1083/jcb.201108113

Ricci, E.P., A. Kucukural, C. Cenik, B.C. Mercier, G. Singh, E.E. Heyer, A. Ashar-Patel, L. Peng, and M.J. Moore. 2014. Staufen1 senses overall transcript secondary structure to regulate translation. *Nat. Struct. Mol. Biol.* 21:26–35. https://doi.org/10.1038/nsmb.2739

Richard, J.W., O.L. Hyun, P. Ina, P. Arun, D. Thom, K. Satoshi, K. Sukhleen, A. Eric Nathaniel, M. Lara, C.M. Anastasia, et al. 2019 Small molecules for modulating protein driven liquid-liquid phase separation in treating neurodegenerative disease. *bioRxiv*. https://doi.org/10.1101/721001 (Preprint posted August 05, 2019).

Roden, C., and A.S. Gladfelter. 2021. RNA contributions to the form and function of biomolecular condensates. *Nat. Rev. Mol. Cell Biol.* 22: 183–195. https://doi.org/10.1038/s41580-020-0264-6

Ross, C.A., and M.A. Poirier. 2004. Protein aggregation and neurodegenerative disease. *Nat. Med.* 10:S10–S17. https://doi.org/10.1038/nm1066

Sardiello, M., M. Palmieri, A. di Ronza, D.L. Medina, M. Valenza, V.A. Gennarino, C. Di Malta, F. Donaudy, V. Embrione, R.S. Polishchuk, et al. 2009. A gene network regulating lysosomal biogenesis and function. *Science*. 325:473–477. https://doi.org/10.1126/science.1174447

Settembre, C., C. Di Malta, V.A. Polito, M. Garcia Arencibia, F. Vetrini, S. Erdin, S.U. Erdin, T. Huynh, D. Medina, P. Colella, et al. 2011. TFEB links autophagy to lysosomal biogenesis. *Science*. 332:1429–1433. https://doi.org/10.1126/science.1204592

Shan, Z., Y. Tu, Y. Yang, Z. Liu, M. Zeng, H. Xu, J. Long, M. Zhang, Y. Cai, and W. Wen. 2018. Basal condensation of Numb and Pon complex via phase transition during Drosophila neuroblast asymmetric division. *Nat. Commun.* 9:737. https://doi.org/10.1038/s41467-018-03077-3

Shirakashi, Y., Y. Kawamoto, H. Tomimoto, R. Takahashi, and M. Ihara. 2006. alpha-Synuclein is colocalized with 14-3-3 and synphilin-1 in A53T transgenic mice. *Acta Neuropathol.* 112:681–689. https://doi.org/10.1007/s00401-006-0132-2

Sugimoto, Y., A. Vigilante, E. Darbo, A. Zirra, C. Militti, A. D'Ambrogio, N.M. Luscombe, and J. Ule. 2015. hiCLIP reveals the in vivo atlas of mRNA secondary structures recognized by Staufen 1. *Nature*. 519:491–494. https://doi.org/10.1038/nature14280

Tabrizi, S.J., R. Ghosh, and B.R. Leavitt. 2019. Huntingtin lowering strategies for disease modification in Huntington's disease. *Neuron*. 101:801–819. https://doi.org/10.1016/j.neuron.2019.01.039

Thomas, M.G., L.J. Martinez Tosar, M.A. Desbats, C.C. Leishman, and G.L. Boccaccio. 2009. Mammalian Staufen 1 is recruited to stress granules and impairs their assembly. *J. Cell Sci.* 122:563–573. https://doi.org/10.1242/jcs.038208

Trettel, F., D. Rigamonti, P. Hilditch-Maguire, V.C. Wheeler, A.H. Sharp, F. Persichetti, E. Cattaneo, and M.E. MacDonald. 2000. Dominant phenotypes produced by the HD mutation in STHdh(Q111) striatal cells. *Hum. Mol. Genet.* 9:2799–2809. https://doi.org/10.1093/hmg/9.19.2799

Vessey, J.P., P. Macchi, J.M. Stein, M. Mikl, K.N. Hawker, P. Vogelsang, K. Wieczorek, G. Vendra, J. Riefler, F. Tübing, et al. 2008. A loss of function allele for murine Staufen1 leads to impairment of dendritic Staufen1-RNP delivery and dendritic spine morphogenesis. *Proc. Natl. Acad. Sci. USA*. 105:16374–16379. https://doi.org/10.1073/pnas.0804583105

Wang, B., H. Martini-Stoica, C. Qi, T.C. Lu, S. Wang, W. Xiong, Y. Qi, Y. Xu, M. Sardiello, H. Li, and H. Zheng. 2024. TFEB-vacuolar ATPase signaling regulates lysosomal function and microglial activation in tauopathy. *Nat. Neurosci.* 27:48–62. https://doi.org/10.1038/s41593-023-01494-2

Wang, Y., C. Yu, G. Pei, W. Jia, T. Li, and P. Li. 2023. Dissolution of oncofusion transcription factor condensates for cancer therapy. *Nat. Chem. Biol.* 19:1223–1234. https://doi.org/10.1038/s41589-023-01376-5

Williams, A., S. Sarkar, P. Cuddon, E.K. Ttofi, S. Saiki, F.H. Siddiqi, L. Jahreiss, A. Fleming, D. Pask, P. Goldsmith, et al. 2008. Novel targets for Huntington's disease in an mTOR-independent autophagy pathway. *Nat. Chem. Biol.* 4:295–305. https://doi.org/10.1038/nchembio.79

Yadav, D.K., D. Zigáčková, M. Zlobina, T. Klumpler, C. Beaumont, M. Kubíčková, Š. Vaňáčová, and P.J. Lukavsky. 2020. Staufen1 reads out structure and sequence features in ARF1 dsRNA for target recognition. *Nucleic Acids Res.* 48:2091–2106. https://doi.org/10.1093/nar/gkz1163

Yu, M., Y. Fu, Y. Liang, H. Song, Y. Yao, P. Wu, Y. Yao, Y. Pan, X. Wen, L. Ma, et al. 2017. Suppression of MAPK11 or HIPK3 reduces mutant Huntingtin levels in Huntington's disease models. *Cell Res.* 27:1441–1465. https://doi.org/10.1038/cr.2017.113

Zhang, H. 2022. The genetics of autophagy in multicellular organisms. *Annu. Rev. Genet.* 56:17–39. https://doi.org/10.1146/annurev-genet-022422-095608

Zhang, H., X. Ji, P. Li, C. Liu, J. Lou, Z. Wang, W. Wen, Y. Xiao, M. Zhang, and X. Zhu. 2020. Liquid-liquid phase separation in biology: Mechanisms, physiological functions and human diseases. *Sci. China Life Sci.* 63:953–985. https://doi.org/10.1007/s11427-020-1702-x

Zhao, Y.G., P. Codogno, and H. Zhang. 2021. Machinery, regulation and pathophysiological implications of autophagosome maturation. *Nat. Rev. Mol. Cell Biol.* 22:733–750. https://doi.org/10.1038/s41580-021-00392-4

Zheng, H., and W. Wen. 2023. Protein phase separation: New insights into cell division. *Acta Biochim. Biophys. Sin.* 55:1042–1051. https://doi.org/10.3724/abbs.2023093

Supplemental material

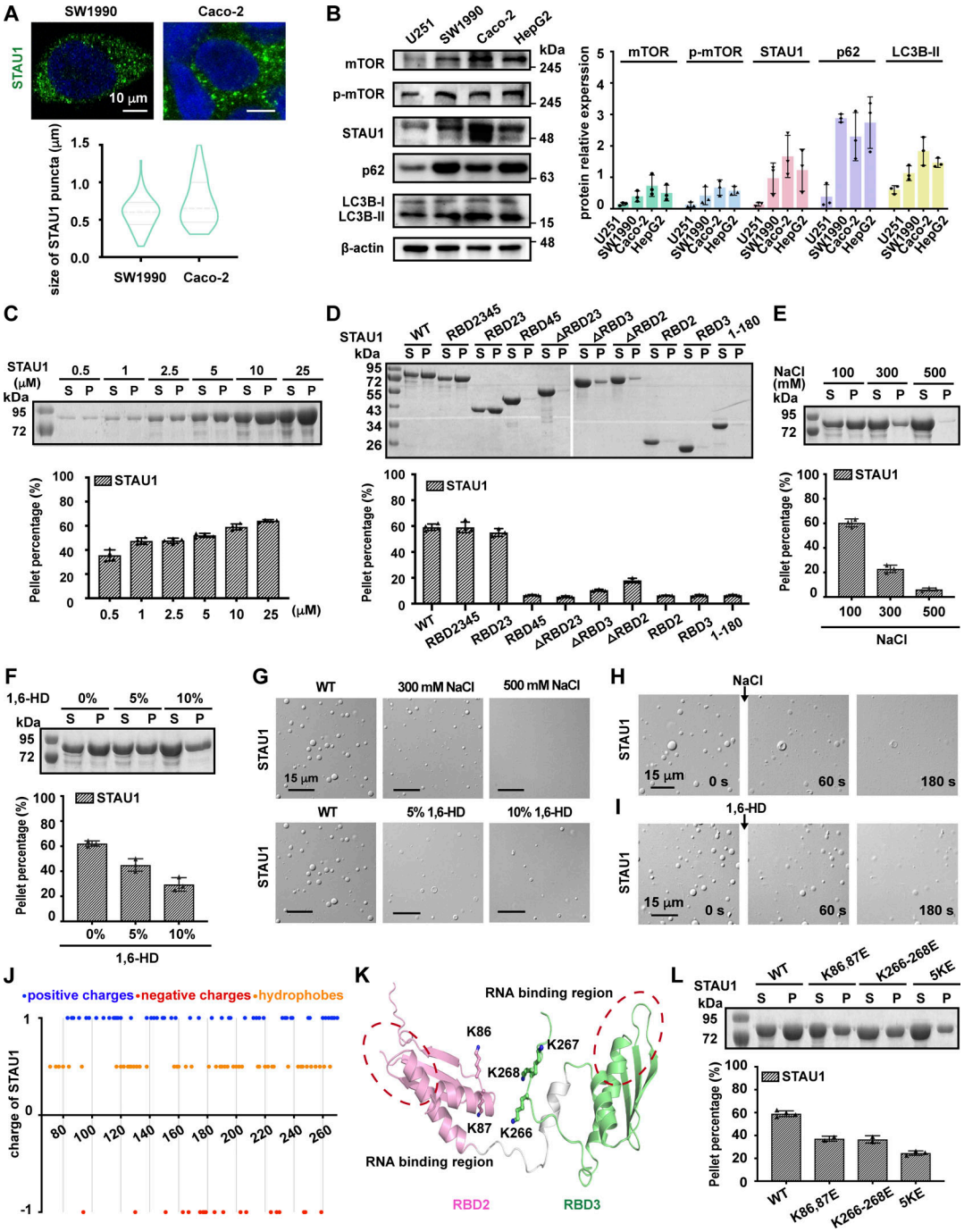

Figure S1. **STAU1 undergoes autonomous phase separation which is mainly driven by electrostatic interactions. (A)** Upper: Representative images of endogenous STAU1 in SW1990 cells and Caco-2 cells. Lower: Statistical data for the sizes of endogenous STAU1 puncta. >150 puncta and >30 cells were counted for each batch. Scale bar: 10 μm. **(B)** Left: Representative immunoblotting images measuring the expression levels of endogenous STAU1, mTOR, and other autophagy markers in various cell lines. Right: Quantitative analysis of the WB assay. The density of each band was normalized by β-actin. **(C)** Upper: Representative sedimentation assay image showing the distribution of proteins between aqueous solution/supernatant (S) and condensed liquid droplets/pellet (P) fractions for STAU1 at various concentrations. Lower: Statistic data for the sedimentation assay. **(D)** Upper: Representative sedimentation assay images showing the distribution of various STAU1 fragments at 10 μM. Lower: Statistic data for the sedimentation assay. **(E and F)** Upper: Representative sedimentation assay images showing STAU1 LLPS (10 μM) could be dramatically or partially blocked by NaCl (E) or 1,6-hexanediol (1,6-HD; F) in a dose-dependent manner. Lower: Statistic data for the sedimentation assay. **(G)** Representative DIC images of STAU1 (10 μM) with increasing amounts of NaCl (upper panel) and 1,6-HD (lower panel). Scale bar: 15 μm. The same sample of STAU1 WT were used in evaluating STAU1 LLPS disruption with salt or 1,6 HD. **(H and I)** Representative time-lapse DIC images showing preformed STAU1 droplets (10 μM) could be dispersed with NaCl (H) or significantly reversed to aqueous phase with 1,6-HD (I). Scale bar: 15 μm. **(J)** Charge and hydrophobe distribution diagram of STAU1. **(K)** Ribbon representation of RBD2 (pink) and RBD3 (green) of STAU1 according to Alphafold prediction. RNA binding regions of RBD domains are highlighted by red dashed ovals and key residues responsible for STAU1 LLPS are shown in the ball-and-stick model. **(L)** Upper: Representative sedimentation assay image of STAU1 and its various mutants at 10 μM. Lower: Statistic data for the sedimentation assay. All statistical data in this figure are expressed as mean ± SD of three or four independent experiments.

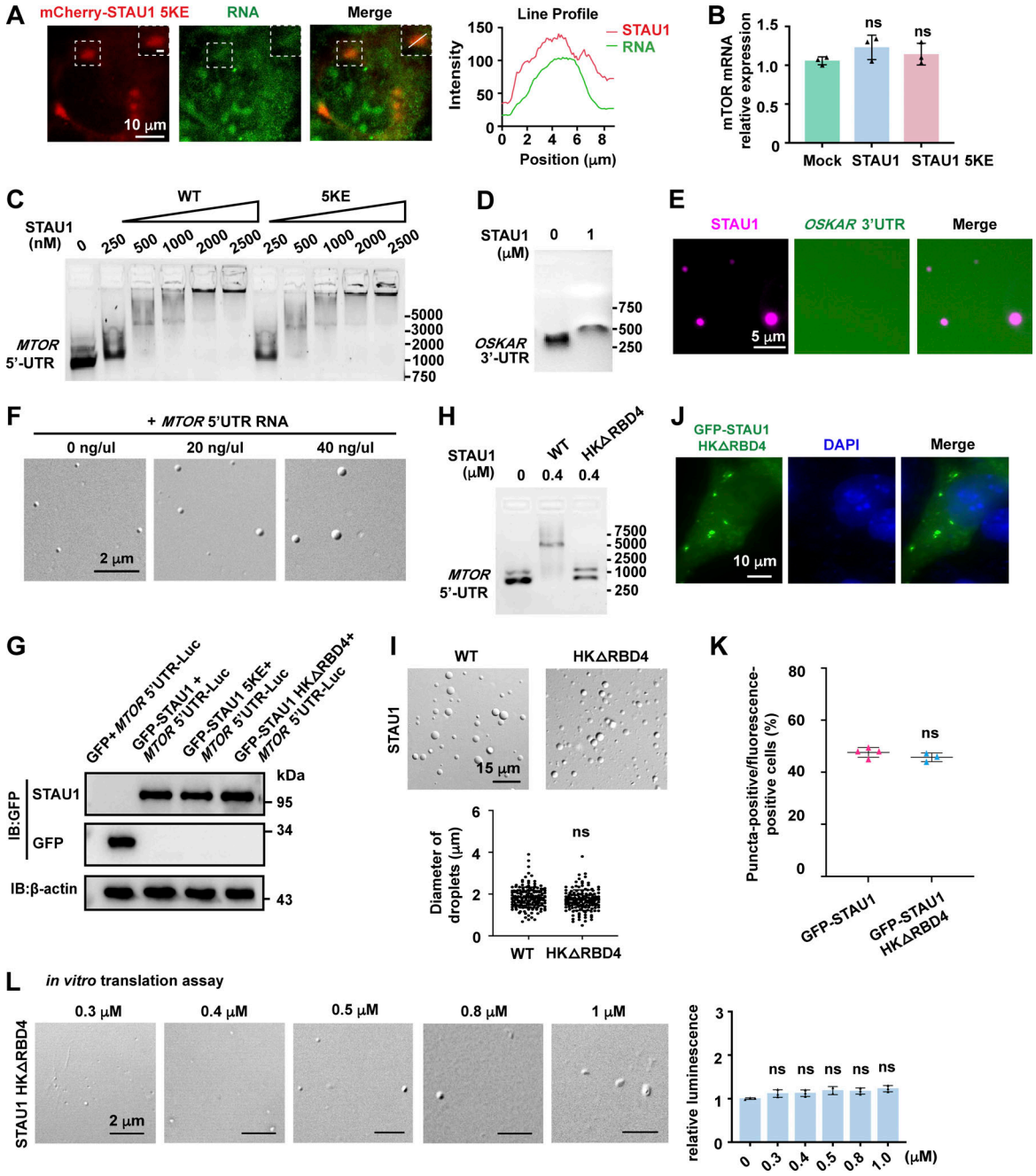

Figure S2. **STAU1 condensate recruits *MTOR* mRNA to enhance its translation. (A)** Left: Representative images showing co-localization of mCherry-STAU1 5KE (red) with RNA (green) within STAU1 5KE condensate (dashed box) in COS7 cells. RNA was stained with SYTO 12 Green-Fluorescent Nucleic Acid Stain. Scale bars, 10 μm; inset, 2 μm. Right: Line plot of STAU1 and RNA fluorescence intensities in indicated box regions. **(B)** *MTOR* mRNA levels in COS7 cells transfected with GFP-STAU1 WT or LLPS-deficient 5KE mutant or the empty vector (Mock) were analyzed by qRT-PCR. RNA expression levels were normalized to GAPDH. **(C)** Representative EMSA assay image of *MTOR* 5′UTR RNA (20 ng) incubated with increasing amounts of STAU1 WT or 5KE mutant in 500 mM NaCl. **(D)** Representative EMSA assay image of *OSKAR* 3′UTR RNA (20 ng) incubated with or without STAU1 (1 μM). **(E)** Representative images showing the droplets of Cy5-STAU1 (5 μM, magenta) could not enrich *OSKAR* 3′UTR (40 ng, green) stained by SYTO12. **(F)** Representative DIC images of STAU1 droplets with the increasing amounts of *MTOR* 5′UTR RNA. Images were acquired at ~3 min after injecting the mixture into the chamber. Scale bar, 2 μm. **(G)** Representative Western blotting images of COS7 cells co-transfected with *MTOR*-5′UTR-LUC reporter and PEGFP-C3, EGFP-STAU1 WT or mutants. **(H)** EMSA assay image of *MTOR* 5′UTR RNA (20 ng) incubated with 0.4 μM of STAU1 WT or HKΔRBD4 mutant. **(I)** Upper: Representative images of STAU1 and STAU1 HKΔRBD4 under DIC microscope at 10 μM. Scale bar: 15 μm. Lower: Scatter plot representing the droplet size of STAU1 and STAU1 HKΔRBD4 at 10 μM. >150 droplets counted for each batch. Data are shown as mean ± SEM; ns, not significant. **(J)** Representative confocal images of exogenously expressed GFP-STAU1 HKΔRBD4 in COS7 cells. Scale bar: 10 μm. **(K)** Statistical data of GFP-STAU1 and GFP-STAU1 HKΔRBD4 puncta formation. Data were collected from three or four independent experimental cell culture batches, >300 cells counted for each batch. Specimens' statistics are presented as mean ± SD; ns, not significant. **(L)** Upper: Representative DIC images of the reaction mixtures with STAU1 HKΔRBD4 mutant after the in vitro translation assay. Protein concentrations of STAU1 HKΔRBD4 are indicated on the top of the panel. Lower: Statistical data for the relative luminescence of different samples. All statistic data are presented as the mean ± SD of three independent experiments; ns, not significant. Source data are available for this figure: SourceData FS2.

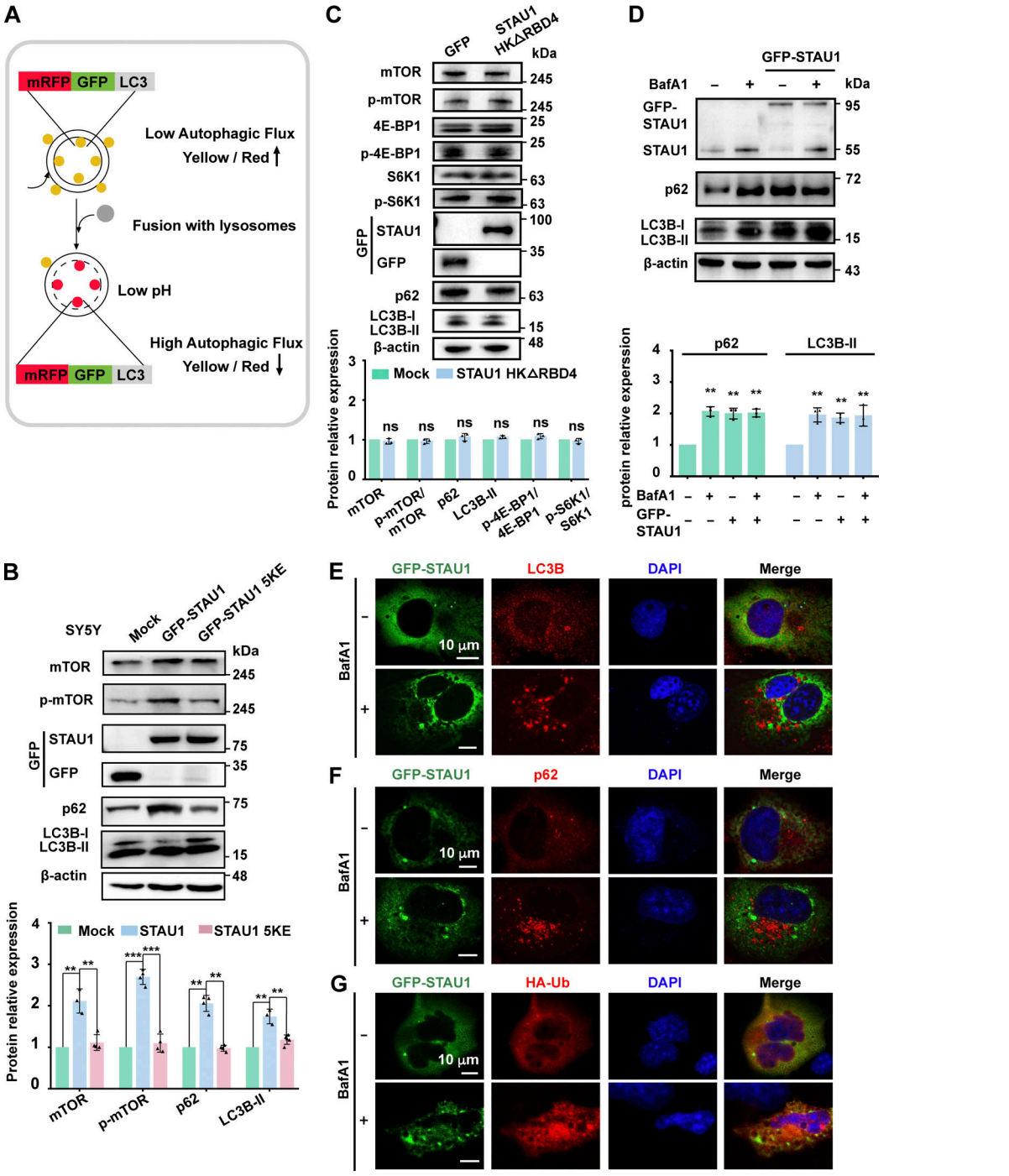

Figure S3. **Overexpressed STAU1 causes defects in autophagosome–lysosome fusion and lysosome function. (A)** Model of mRFP-GFP-LC3 tandem fluorescent protein quenching assay. mRFP-GFP-LC3 emits both green and red fluorescence signals when the protein localizes to autophagosomes, showing yellow signals in merged images. Upon fusion with lysosomes, GFP fluorescence is quenched due to the low pH of lysosomes, whereas mRFP fluorescence is stable, and the puncta becomes GFP-negative/mRFP-positive (red). **(B)** Upper: Representative Western blotting images of mTOR, p-mTOR, p62, and LC3B-II levels in SH-SY5Y cells expressing PEGFP-C3, GFP-STAU1 WT, or 5KE. Lower: Statistic graph of quantified fold changes. Levels of mTOR and other autophagy-related proteins are normalized to β-actin. Experiments were performed more than three times independently with similar results. **(C)** Upper: Representative WB images of mTOR, p-mTOR, p62, 4EBP1, p-4EBP1, S6K1, p-S6K1, and LC3B-II levels in COS7 cells exogenously expressing control PEGFP-C3 or GFP-STAU1 HKΔRBD4. Lower: Statistic graph of quantified fold changes. **(D)** Upper: Representative immunoblotting images measuring the expression levels of endogenous STAU1 and autophagy markers in COS7 cells and COS7 cells transfected with GFP-STAU1 with or without BafA1 treatment (100 nM). Lower: Statistic graph of quantified fold changes. The density of each band was normalized by β-actin. **(E–G)** COS7 cells transiently transfected with 0.8 μg GFP-STAU1 (E and F) or together with HA-Ub (G) with or without treatment of the autophagy inhibitor BafA1 (100 nM for 6 h) were stained with anti-LC3B (E), anti-p62 (F), or anti-HA (G). Scale bar: 10 μm. All specimens' statistics in this figure represent the results from three independent batches of experiments are presented as mean ± SD; ns, not significant, *P < 0.05, **P < 0.01, ***P < 0.001 using one-way ANOVA with Tukey's multiple comparison test. Source data are available for this figure: SourceData FS3.

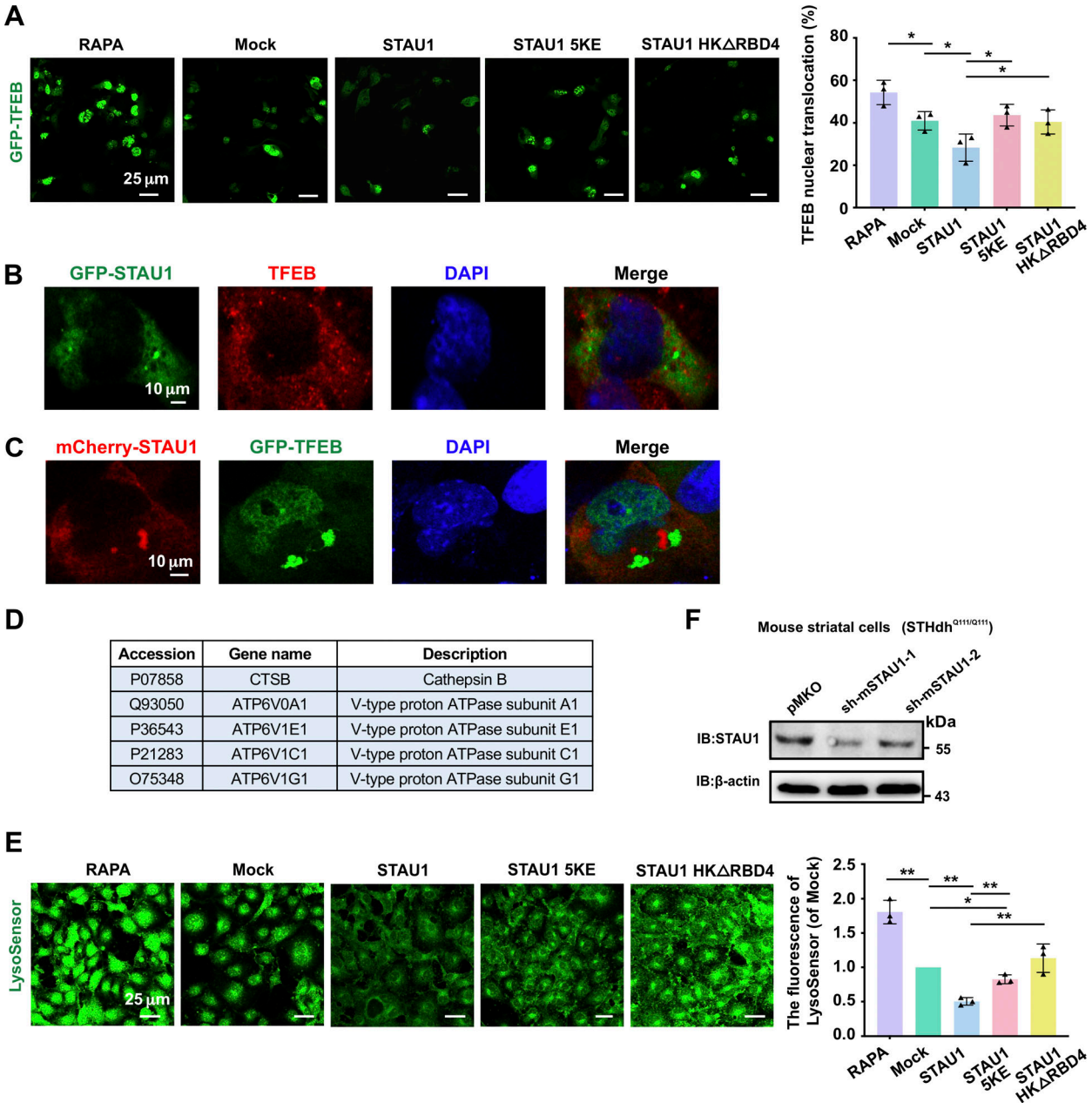

Accession	Gene name	Description
P07858	CTSB	Cathepsin B
Q93050	ATP6V0A1	V-type proton ATPase subunit A1
P36543	ATP6V1E1	V-type proton ATPase subunit E1
P21283	ATP6V1C1	V-type proton ATPase subunit C1
O75348	ATP6V1G1	V-type proton ATPase subunit G1

Figure S4. **STAU1 overexpression impairs TFEB translocation and lysosome acidification. (A)** Left: Representative images showing the distribution of TFEB in COS7 cells coexpressing GFP-TFEB with mCherry-vector, mCherry-STAU1 WT, 5KE mutant, or HKΔRBD4 mutant. Untransfected cells were treated with 100 nM rapamycin. Right: Quantification of the number of cells with nuclear TFEB localization. Scale bar, 25 μm. Data were collected from three independent experimental cell culture batches, with >300 cells counted for each batch. **(B)** COS7 cells were transiently transfected with GFP-STAU1 and stained with anti-TFEB (red). **(C)** mCherry-STAU1 and GFP-TFEB were co-transfected into COS7 cells. Scale bar: 10 μm. **(D)** List of downregulated TFEB downstream targets identified by mass spectrometry analysis (fold change ~0.6). **(E)** Representative images and quantification of LysoSensor Green DND-189 staining in COS7 cells transfected with PEGFP-C3, GFP-STAU1 WT, 5KE, and HKΔRBD4. Scale bar, 25 μm. Data were collected from three independent experimental cell culture batches, with >300 cells quantified for each batch. **(F)** Representative Western blotting images of STAU1 levels in STHdh$^{Q111/Q111}$ cells transduced with mSTAU1 shRNAs (sh-mSTAU1-1 and sh-mSTAU1-2) or pMKO vector lentiviruses. STAU1 expression level was dramatically decreased in sh-mSTAU1-1 depleted cells. All statistic data are presented as mean ± SD; *P < 0.05, **P < 0.01 using one-way ANOVA with Tukey's multiple comparison test (not significant difference was not marked). Source data are available for this figure: SourceData FS4.

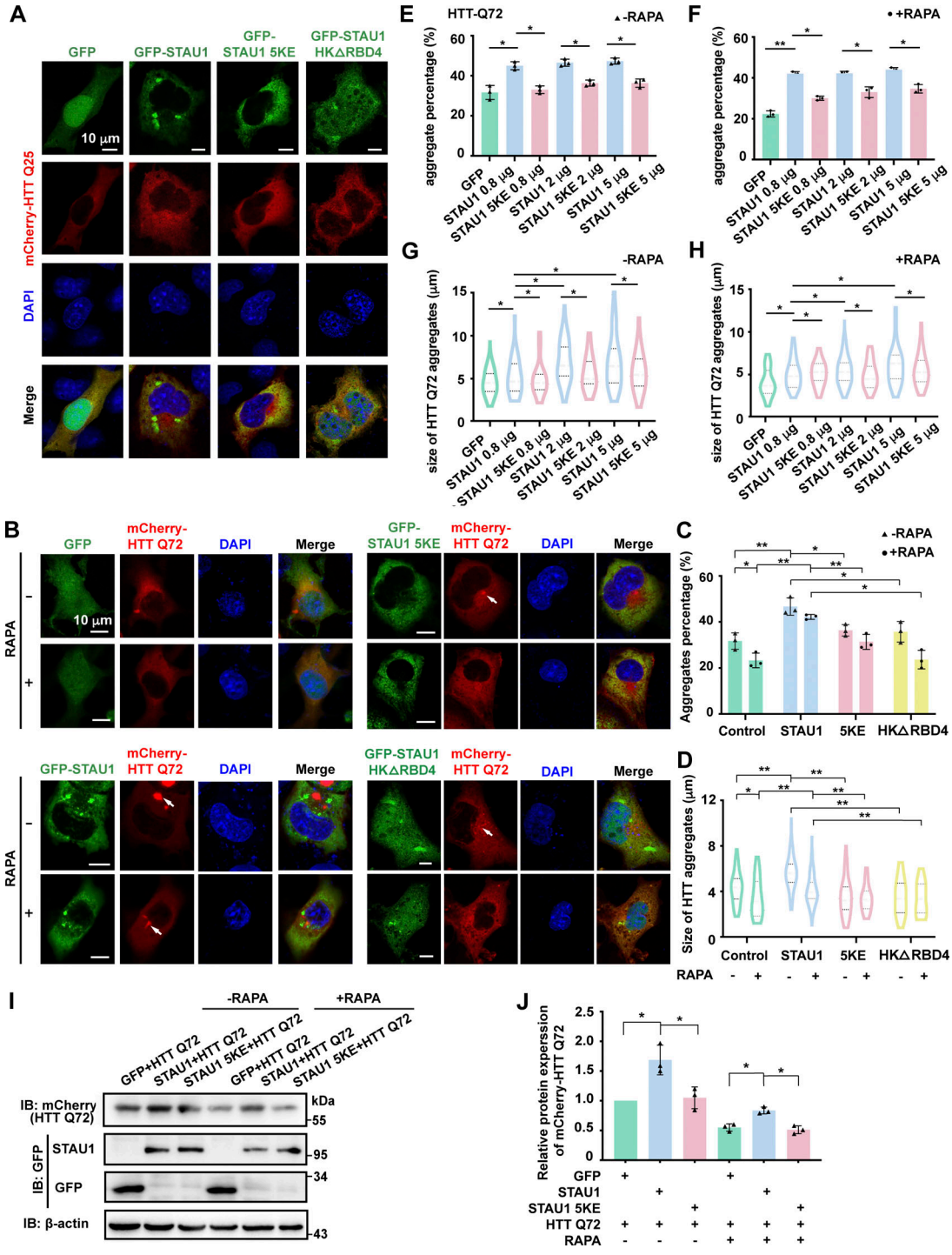

Figure S5. **LLPS of STAU1 promotes mutant HTT aggregation in the cellular HD model. (A)** Representative images showing co-expression of mCherry-HTTexon1 Q25 and PEGFP-C3, EGFP-STAU1 WT, 5KE mutant or HKΔRBD4 mutant in COS7 cells. **(B)** Representative confocal images showing co-expression of mCherry-HTTexon1 Q72 with control PEGFP-C3, EGFP-STAU1 WT, 5KE mutant, or HKΔRBD4 mutant in COS7 cells. The mCherry-HTTexon1 Q72 transfected cells were treated with 1 μmol/l rapamycin to stimulate autophagy. **(C)** Statistical data for the population of cells containing HTT Q72 aggregates. **(D)** Statistical data for the sizes of HTT Q72 aggregates. Data were collected from three independent experimental cell culture batches, with >200 cells counted for each batch. **(E–H)** COS7 cells were co-transfected with mCherry-HTTexon1 Q72 and increasing amounts of GFP-STAU1 plasmid (from 0.8 to 5 μg per well in a 12-well plate). The transfected cells were treated with 1 μmol/l rapamycin to stimulate autophagy. Statistical data of the population of cells containing HTT Q72 aggregates in COS7 cells without or with rapamycin treatment are presented in E and F, respectively. >300 cells were counted for each batch. Statistical data of the size of HTT Q72 aggregates without or with rapamycin treatment are presented in G and H, respectively. **(I)** Representative Western blot images of HTT Q72 in COS7 cells coexpressing mCherry-HTTexon1 Q72 and control GFP-vector, EGFP-STAU1 WT, or 5KE mutant. **(J)** Quantification of Western blotting bands in I for the indicated proteins using β-actin abundance for normalization and presented as fold changes. All specimens' statistics in this figure represent the results from three independent batches of experiments are presented as mean ± SD; *P < 0.05, **P < 0.01 using one-way ANOVA with Tukey's multiple comparison test. Source data are available for this figure: SourceData FS5.

Provided online are Table S1 and Table S2. Table S1 is a list of selected upregulated proteins in U251 cells overexpressing STAU1 WT rather than LLPS-deficient 5KE mutant identified by mass spectrometry analysis (fold change >2, ranking in the top 40). Table S2 is a list of selected downregulated proteins in U251 cells overexpressing STAU1 WT rather than LLPS-deficient 5KE mutant identified by mass spectrometry analysis (fold change <0.5, ranking in the top 40).